



# Methane retrieval from airborne HySpex observations in the short-wave infrared

Philipp Hochstaffl<sup>1</sup>, Franz Schreier<sup>1</sup>, Claas Henning Köhler<sup>1</sup>, Andreas Baumgartner<sup>1</sup>, and Daniele Cerra<sup>1</sup>

<sup>1</sup>Deutsches Zentrum für Luft- und Raumfahrt, Institut für Methodik der Fernerkundung, 82234 Oberpfaffenhofen, Germany

**Correspondence:** Philipp Hochstaffl (philipp.hochstaffl@dlr.de)

**Abstract.** A reduction of methane emissions could help to mitigate global warming on a relatively short time scale. Monitoring of local and regional anthropogenic CH<sub>4</sub> emissions is crucial in order to increase our understanding of the methane budget which is still subject to scientific debate.

The study compares various retrieval schemes that estimate localized CH<sub>4</sub> emissions from ventilation shafts in the Upper Silesian Coal Basin (USCB) in Poland using short-wave infrared nadir observations of the airborne imaging spectrometer HySpex. The examined methods are divided into nonlinear and linear schemes. The former class are of iterative nature and encompass various nonlinear least squares setups while the latter are represented by the Matched Filter (MF), Singular Value Decomposition (SVD) and Spectral Signature Detection (SSD) algorithms. Particular emphasis is put on strategies to remedy the problem of albedo related biases due to correlation with broad band absorption features caused by the hyperspectral instrument's low spectral resolution.

It was found that classical nonlinear least squares fits based on the Beer InfraRed Retrieval Algorithm (BIRRA) suffers from surface-type dependent biases. The effect is more pronounced for retrievals from single spectral intervals but can be mitigated when multiple intervals are combined. The albedo related correlation is also found in the BIRRA solutions for the separable least squares. A new BIRRA setup that exploits the inverse of a scene's covariance structure to account for reflectivity statistics significantly reduces the albedo bias and enhances the CH<sub>4</sub> signal so that the method infers two- to threefold higher methane concentrations.

The linear estimators turned out to be very fast and well suited to detect enhanced levels of methane. The linearized BIRRA forward model turned out to be sensitive to the selected retrieval interval and in the default setup only works for very narrow windows. Other well established linear methods such as the MF and SVD identified the methane pattern as well and largely agree with the BIRRA fitted enhancements hence the methods allow quantitative estimates of methane. The latter two methods yielded increased performance when the scene was further divided into clusters by applying k-means in a preprocessing step. Methane plumes detected with the simple SSD method were faint and found rather sensitive to the polynomial used to compute the method's residuum ratio.



## 1 Introduction

25 Methane ( $\text{CH}_4$ ) is the second most important greenhouse gas next to carbon dioxide ( $\text{CO}_2$ ) according to the latest IPCC report (Masson-Delmotte et al., 2021). Due to its comparatively short lifetime of approximately 9 years, a reduction of methane emissions could help to mitigate global warming on a relatively short time scale of approximately one decade. Despite improvements in monitoring regional and global  $\text{CH}_4$  emissions in recent years the IPCC report points out that fundamental uncertainties pertaining to the methane budget remain (Intergovernmental Panel on Climate Change, 2014).

30 Observations indicate an increasing trend in atmospheric  $\text{CH}_4$  content since 2007, the cause of which is still subject to scientific debate. The vast majority of anthropogenic  $\text{CH}_4$  emissions is caused by small scale phenomena such as agriculture (enteric fermentation & manure), waste management (landfills) and fossil fuel exploitation, where the latter is responsible for 20-30 % of all anthropogenic  $\text{CH}_4$  emissions. Consequently there exists the need for continuous long-term methane observations on a global scale, in order to foster understanding on the global methane cycle, devise future reduction measures and  
35 monitor their effectiveness. The monitoring of anthropogenic emissions of  $\text{CH}_4$  and  $\text{CO}_2$  is also part of the United Nations Framework Convention on Climate (2015) as nationally determined contributions should be assessed via global stock takes on a 5 year basis from 2023 (Article 13 & 14 of the Paris Agreement).

Satellite observations are typically the method of choice for such continuous and global long-term observations. Space-borne spectrometers measuring short-wave infrared (SWIR) solar radiation reflected at the Earth surface are especially well suited to  
40 observe atmospheric  $\text{CH}_4$  in the lower atmosphere by measuring its absorption in the bands 1560-1660 nm and 2090-2290 nm. In contrast, the thermal infrared is less sensitive to variations in  $\text{CH}_4$  concentration close to the surface. Moreover, thermal sensors often have lower spatial resolution making them less favorable for emission monitoring (Richter, 2010).

Operational  $\text{CH}_4$  products from contemporary atmospheric composition missions such as TROPOMI (TROPOspheric Monitoring Instrument; Veefkind et al. (2012)), GOSAT/GOSAT-2 (Greenhouse gases Observing SATellite; Kuze et al. (2009, 2016))  
45 measure trace gas concentrations with very high accuracy, nevertheless, they are not optimally suited to measure emissions of point-like sources. This design inherent limitation is due to their focus on rapid global coverage, which entails a comparatively coarse spatial resolution of several square kilometers per pixel. Since the emission of a single point source inside a pixel is averaged over the entire resolution cell, even large sources seldomly elevate the mean  $\text{CH}_4$  concentration within one pixel by more than one percent compared to the undisturbed background (Lauvaux et al., 2022). A way to increase the contrast  
50 of enhancements is to operate typical atmospheric remote sensing spectrometers at lower altitudes (e.g. on aircraft), thus increasing the spatial resolution while leaving the overall optical design untouched. This strategy is followed by instruments such as MAMAP/MAMAP-2D (Gerilowski et al., 2011) or GHOST (Humpage et al., 2018) which are very well suited for the calibration and validation of their space-borne counterparts.

In order to increase the sensitivity towards smaller sources an increased spatial resolution is required, which in turn necessitates a trade-off in spectral resolution because the loss of photons caused by the smaller emitting area per pixel reduces  
55 the Signal-to-Noise Ratio (SNR) of the image which has to be compensated by broadening the spectral interval per spectral channel. Imaging spectrometers for land surface remote sensing (often referred to as hyperspectral cameras) are typical exam-





60 ples of instruments optimized for spatial resolution this way. Their technology matured over the last 30 years and a variety of  
airborne instruments and several space-borne versions are either in orbit (PRISMA, Guanter et al., 2021; ENMAP, Chabrillat  
et al., 2020) or going to be launched in the future (CHIME). Yet other sensors dedicated for the detection of methane (GHGSat,  
Jervis et al., 2021) and carbon dioxide (e. g., Carbon Mapper, CO2Image) have slightly higher spectral resolution than their  
hyperspectral counterparts but still offer a much higher spatial resolution than atmospheric composition missions.

65 Thorpe et al. (2013) were the first to demonstrate that localized CH<sub>4</sub> emissions over land can be detected from hyperspectral  
cameras with the Airborne Visible/Infrared Imaging Spectrometer (AVIRIS, Green et al. 1998) and that a limited quantitative  
analysis is possible (Thorpe et al., 2014). Similar studies were repeated with airborne instruments (AVIRIS-NG, Borchardt  
et al. 2021; HySpex, Nesme et al. 2020) and space-borne instruments (Thompson et al., 2016; Guanter et al., 2021). Works  
by Varon et al. (2019); Jervis et al. (2021) demonstrated that CH<sub>4</sub> sources can even be detected with the multi-spectral MSI  
instrument on-board the Sentinel-2 satellites, but these measurements are restricted to 'favourable conditions' (i. e., strong  
sources and high surface albedo).

70 One of the core challenges when retrieving methane from measurements with high spatial and moderate spectral resolution  
(> 1 nm) is the separation of spectral variations caused by molecular absorption and surface reflectivity. Classical trace gas  
retrievals for high-spectral resolution instruments such as RemoteC (Lorente et al., 2021), Weighting Function Modified Dif-  
ferential Optical Absorption Spectroscopy (WFM-DOAS, Buchwitz et al., 2005), or the Beer InfraRed Retrieval Algorithm  
(BIRRA, Gimeno García et al., 2011) exploit the high frequency characteristics of gaseous absorption and attribute the smooth  
75 varying part to the surface albedo. Instruments with coarse spectral resolution, however, are unable to sufficiently resolve those  
molecular signatures which causes ambiguities that often leads to surface-type related biases in the 'classical' retrieval schemes  
(e. g., Borchardt et al., 2021, Sec. 3.3 or Thorpe et al., 2014, Sec. 9.2). Alternative more 'data-driven' retrieval schemes such  
as the Matched Filter (MF) or the Singular Value Decomposition (SVD) estimate enhancements based on methods from linear  
algebra and statistics (Thorpe et al., 2013; Thompson et al., 2015; Thorpe et al., 2014).

80 This study compares various retrieval schemes applied to measurements from DLR's (German Aerospace Centre) HySpex  
sensor system and the paper is structured as follows. The next section briefly describes the experimental setup, provides a quick  
review of atmospheric radiation, and introduces the various BIRRA setups that were examined in this study. Thereafter, other  
(simpler but faster) retrieval schemes employed in this work are briefly described. The result section starts with a feasibility  
analysis for BIRRA with (simulated) HySpex data and proceeds with the presentation of the retrieval results from HySpex  
85 observations for different BIRRA setups over the Pniowek V ventilation shaft. Thereafter, the results from the well established  
'data driven' fitting techniques such as MF and SVD, are presented. In the last chapter, results are summarized and put into  
perspective.

## 2 Methodology

90 Methods introduced in this section can be divided into linear and nonlinear schemes. While the former are very fast and often  
of sufficient accuracy the nonlinear iterative solvers require more computing power and hence time to come up with a best



estimate. The retrieval methods are tailored to remedy the problem of albedo related biases due to correlation with broad band absorption features caused by the instrument's low spectral resolution.

## 2.1 Experimental Setup

The measured spectra analyzed in the study at hand were acquired during the COMET (Carbon diOxide and METHane) campaign with the DLR HySpex sensor system. This airborne imaging spectrometer, which consists of two commercially available hyperspectral cameras (a VNIR-1600 and a SWIR-320m-e) is described in detail in (IMF) and references therein.

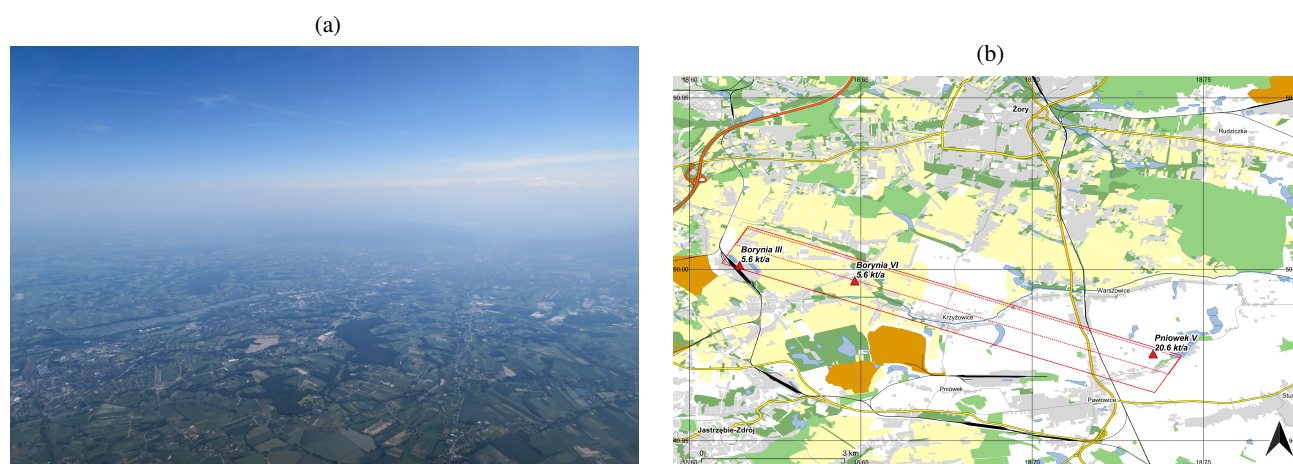


**Figure 1.** (a) View from the aircraft into the mountains around Zywiec at 10 UTC on June 07, 2018. (b) In the depicted flight track ("scene 09") the aircraft was on a 115 degrees eastbound heading at  $\approx 1.5$  km above mean sea level. The map was created with QGIS using OpenStreetMap data (© OpenStreetMap contributors, 2022).

The data analyzed in the following chapters was collected during a survey flight conducted within the scope of the CoMet campaign on June 7th, 2018. The CoMet campaign focused on the detection and characterization of  $\text{CO}_2$  and  $\text{CH}_4$  sources in the Upper Silesian Coal Basin in southern Poland. It featured a number of ground-based and airborne measurements with both in-situ and remote sensing instruments. The HySpex survey was intended as a feasibility study to evaluate whether – and if so how accurate – localized methane emissions can be retrieved from the SWIR-320m-e data. To achieve this goal we planned 18 flight lines at two different altitudes over a number of known ventilation shafts around Katowice. The location and estimated emission rate of the ventilation shafts was taken from the CoMet ED v1 inventory assembled by Nickl et al. (2020). It was not known in advance, though, which of these ventilation shafts would be actively emitting methane during the day of the survey, as the emission rates are derived from monthly averages reported by the mining companies operating the shafts. The weather during the survey was well suited for remote sensing measurements. Apart from very few occasional patches of thin cirrus clouds there were no further low or mid-level clouds. However, a significant amount of haze could be observed from the aircraft. This can be seen in Image 1a, which displays a view from the aircraft towards the mountains around Bielsko-Biala,



located approximately 20 km southeast of the survey area. Actual wind data for the USCB area on the measurement day is  
110 presented in Luther et al. (2022, Fig. 4 and 6).

Since this study compares the performance of various retrieval methods, we restrict our analysis to the two flight lines: Flight  
line 9, acquired at 1200 m above ground level (AGL) around 0955 UTC and flight line 11 acquired at 2600 m AGL around  
1010 UTC. The respective foot prints of line 9 (dashed red line) and line 11 (solid red line) are shown in Fig. 1b along with the  
location and estimated emission rate of the three ventilation shafts (red triangles) located within. Each track took the aircraft  
115  $\approx 3$  minutes during which 7130 (scene 09) and 5075 (scene 11) along track observations for each of the 320 across track  
detector pixels were acquired.

In Fig. 2b an ensemble of along track averaged HySpex measurements are depicted. The sensor's sampling distance across  
the spectral axis is indicated by the vertical grid lines which is not constant in the wavenumber domain. The spectral coverage  
of the HySpex SWIR-320m-e camera ranges from 967–2496 nm ( $4005\text{--}10338\text{ cm}^{-1}$ ), with the exact number depending on the  
120 across track pixel ( $\approx \pm 1\text{ cm}^{-1}$ ). The spectral resolution, i. e., the full width at half maximum (FWHM) of the HySpex SWIR-  
320m-e camera in the  $4000\text{--}6500\text{ cm}^{-1}$  region ranges from 6.0–9.5 nm ( $10\text{--}40\text{ cm}^{-1}$ ). Its values are provided for each across  
track pixel of the detector (a 2D array) with the level 1b data set. This data set was basically created as described in Lenhard  
et al. (2015), except for the optical distortion correction. The Instrument Spectral Response Function (ISRF) calibration was  
performed according to Baumgartner (2021). Hence, the ISRF for each pixel is available as a lookup table with an sampling  
125 distance of 1.2 nm. The standard HySpex product is corrected for optical distortions and resampled to a constant spectral  
resolution and across-track resolution using the method described in Baumgartner and Köhler (2020). For this study, this  
processing step was omitted.

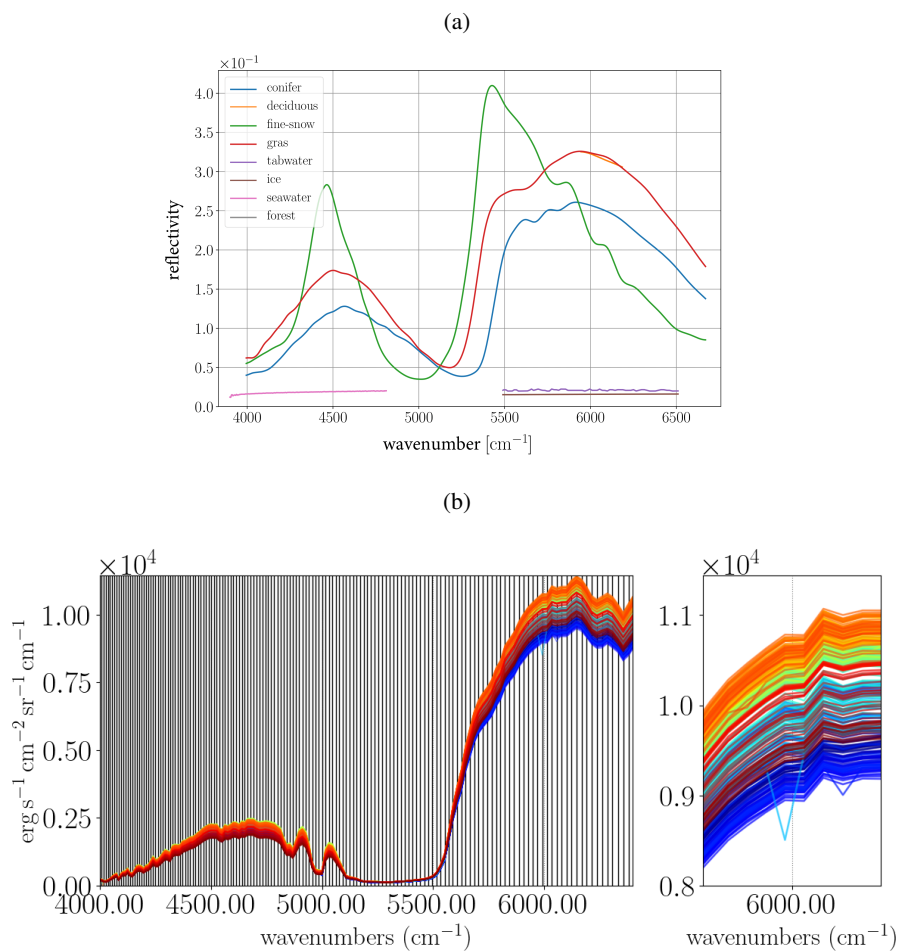


**Figure 2.** (a) Reference reflectances for different surface types (measured at the John Hopkins University). (b) HySpex measurements across the 320 detector pixels (from blue to red, left to right). The radiance values of across track pixel 104 (cyan) for wavenumber  $5960 \text{ cm}^{-1}$  (relevant for the  $\text{CH}_4$  retrieval) appear to be problematic.

As pointed out, it is the rather low spectral resolution that makes the retrieval of atmospheric constituents challenging. Figure 2 shows reflectances for various surface types along track averaged HySpex spectra. Note that the radiative intensity in the interval around  $6000 \text{ cm}^{-1}$  is significantly larger compared to the radiance between  $4000\text{--}5000 \text{ cm}^{-1}$ . The measurement is only able to resolve broad band molecular absorption features since the high frequency variations are smoothed by the coarse instrument resolution (see absorption from methane's  $2\nu_3$  band around  $6000 \text{ cm}^{-1}$ ). The figure also indicates a possible bad pixel with systematically lower radiance values along the flight track, just below  $6000 \text{ cm}^{-1}$ , corresponding to across track pixel 104 (a descending cyan line).



## 135 2.2 Radiative transfer

In the SWIR spectral range the radiative transfer for a down and up path through the atmosphere under clear sky conditions (cloud free) is well described by Beer's law (Zdunkowski et al., 2007) with the monochromatic transmission from Top of Atmosphere (TOA) to Bottom of Atmosphere (BOA) given by

$$T_m(\nu; s) = \exp\left(-\sum_m \tau_m(\nu, s) ds\right) = \exp\left(-\int_{\text{path}} ds \sum_m n_m(s) k_m(\nu, p(s), T(s))\right). \quad (1)$$

140 The model assumes a pure gas atmosphere with molecular optical depth  $\tau$  given by the path integral over the molecular number densities  $n_m$  and  $k_m$ , the pressure and temperature dependent absorption cross section.

In conditions where particles such as haze, dust or high clouds prevail, extinction (scattering and absorption) by aerosols should be taken into account (De Leeuw et al., 2011). Aerosol optical thickness  $\tau_{\text{aer}}$  at wavenumber  $\nu$  is often described by a power law

$$145 \tau_{\text{aer}}(\nu) = \tau_{\text{aer}}(\nu_0) \left(\frac{\nu}{\nu_0}\right)^\beta, \quad (2)$$

where  $\tau_{\text{aer}}(\nu_0)$  is the optical thickness at a reference wavenumber and  $\beta$  a parameter for the aerosol. The Ångström exponent  $\beta$  typically ranges from  $1 \leq \beta \leq 2$  (Liou, 2002) and while it is close to 1.0 for almost clear sky conditions with weak scattering by haze or dust, it is assumed to increase for hazy conditions. In analogy to  $k_m$  the aerosol cross section can be defined as

$$\tau_{\text{aer}}(\nu_0) = \int_{\text{path}} k_{\text{aer}}(\lambda_0) n_{\text{air}}(s) ds = N_{\text{air}} k_{\text{aer}}(\lambda_0) (10^4/\nu)^{-\beta} \quad (3)$$

150 with  $\lambda_0 = 1 \mu\text{m}$  and  $k_{\text{aer}}(\nu)$  proportional to  $\lambda^{-\beta}$  according to

$$k_{\text{aer}}(\lambda) = k_{\text{aer}}(\lambda_0)/\lambda^\beta \quad \text{and} \quad k_{\text{aer}}(\lambda_0) = 1.4 \cdot 10^{-27}. \quad (4)$$

## 2.3 Model atmosphere setup

The model atmosphere's vertical extent ranges from 0–80 km with 39 levels in total. The atmosphere is composed by pure gaseous layers above  $z_{\text{mol}} = 10$  km and layers containing gases and particles below  $z_{\text{sc}} = 10$  km. The vertical resolution is  
 155 highest in the (plume) layer below  $z_{\text{pl}} = 2$  km where the enhancement is expected to take place (see Fig. 3). The  $\text{CH}_4$  optical depth is modeled in terms of a climatological background and a Gaussian plume

$$\tau_{\text{CH}_4} = \tau_{\text{bg}} + \alpha_{\text{CH}_4} \tau_{\text{pl}}. \quad (5)$$

Although the shape of the plume profile is not crucial as the nadir viewing geometry does not allow to retrieve information on the vertical distribution of trace gases in the SWIR (see Buchwitz et al. (2000, Sec. 3)) our setup constrains the fit to the lowest  
 160 atmospheric layer up to 2.0 km (see Thorpe et al. (2014, 5.2)).



The CH<sub>4</sub> background as well as the CO<sub>2</sub> initial guesses are modeled according to the Air Force Geophysical Laboratory (AFGL, Anderson et al., 1986) atmospheric constituent profiles scaled to 1875 ppb and 400 ppm, respectively. The molecules H<sub>2</sub>O as well as the auxiliary parameters temperature and pressure are taken from reanalysis data provided by the National Center for Environmental Prediction (NCEP, Kalnay et al., 1996).

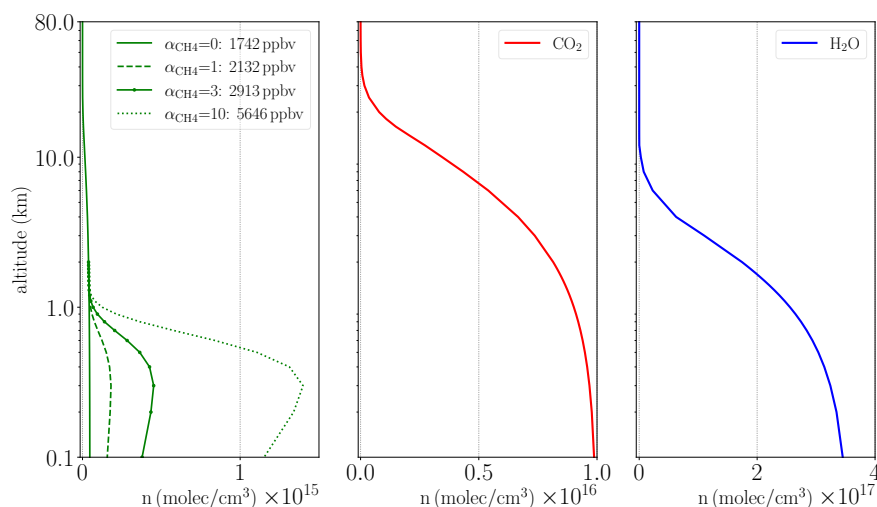


**Figure 3.** Atmospheric vertical profiles of molecular number densities  $n_m$  for CH<sub>4</sub>, CO<sub>2</sub>, and H<sub>2</sub>O. The CH<sub>4</sub> profile is split into two components, i. e., a reference (background) profile ranging from BoA to ToA and a Gaussian plume enhancement < 2 km which is scaled by  $\alpha_{\text{CH}_4}$ . Beside CH<sub>4</sub> the well mixed CO<sub>2</sub> profile is depicted in the middle while an initial guess for H<sub>2</sub>O is shown on the right.

## 165 2.4 Beer InfraRed Retrieval Algorithm (BIRRA)

The BIRRA level 2 processor was originally developed at the Deutsches Zentrum für Luft- und Raumfahrt (DLR) and comprises the line-by-line forward model Generic Atmospheric Radiation Line-by-line InfraRed Code (GARLIC, Schreier et al., 2014) coupled to a least squares solver for trace gas retrieval in the SWIR spectral region (Hochstaffl et al., 2018). It has been successfully applied to SCIAMACHY (Scanning Imaging Absorption Spectrometer for Atmospheric Chartography, Gimeno  
 170 García et al., 2011; Hochstaffl and Schreier, 2020) and TROPOMI (TROPOspheric Monitoring Instrument, Hochstaffl et al., 2020) observations. The BIRRA retrievals in this study are based on a Python reimplementaion of the validated (Fortran) code (Gimeno García et al., 2011; Hochstaffl et al., 2018). The radiative transfer computations are hence based on Py4CATS (Python for Computational Atmospheric Spectroscopy, (Schreier et al., 2019)), a Python reimplementaion of GARLIC.

The mathematical forward model  $\Phi(\mathbf{x}, \nu)$  describes the measured intensity spectrum  $I(\nu)$  for a nadir looking observer  
 175 according to

$$\Phi(\mathbf{x}, \nu) = \frac{r(\nu)}{\pi} \cos(\theta) I_{\text{sun}}(\nu) \mathcal{T}_m^\downarrow(\nu) \mathcal{T}_m^\uparrow(\nu) \otimes S(\gamma(\nu)), \quad (6)$$



where  $r$  refers to the surface reflectivity and  $\theta$  represents the solar zenith angle. The terms  $\mathcal{T}_m^\downarrow$  and  $\mathcal{T}_m^\uparrow$  denote the total transmission between Sun and reflection point (e.g. the Earth) and between reflection point and observer (e.g. the HySpex sensor), respectively. The transmission by aerosols for different Ångström exponents according to Eq. (2) is depicted in Fig. 4 (center).

180 Its behavior can be represented by a low order polynomial hence the forward's model total transmission is described as

$$\mathcal{T}_m(\nu; s) = \exp\left(-\sum_m \alpha_m \tau_m(\nu) - \sum_{i>0} a_i \nu^i\right). \quad (7)$$

The unknown (to be estimated) parameters are composed as elements of the state vector  $\mathbf{x}$  and include the molecular scaling factors  $\alpha_m$ , the aerosol coefficients  $a_i$ , and the coefficients for the surface reflectivity  $r_j$  (with  $j \geq 0$ ) which is also modeled by a polynomial. Note that since the information of the vertical profile is well under-determined in the observed spectrum scaling

185 factors  $\alpha_m$  for the initial guess profiles are retrieved (Gimeno García et al., 2011, Fig. 1). Finally, the instrument's spectral response is described by the spectral response function (SRF)  $S$ . Its parameters such as the half width  $\gamma$  or a spectral shift can (optionally) be part of the state vector.



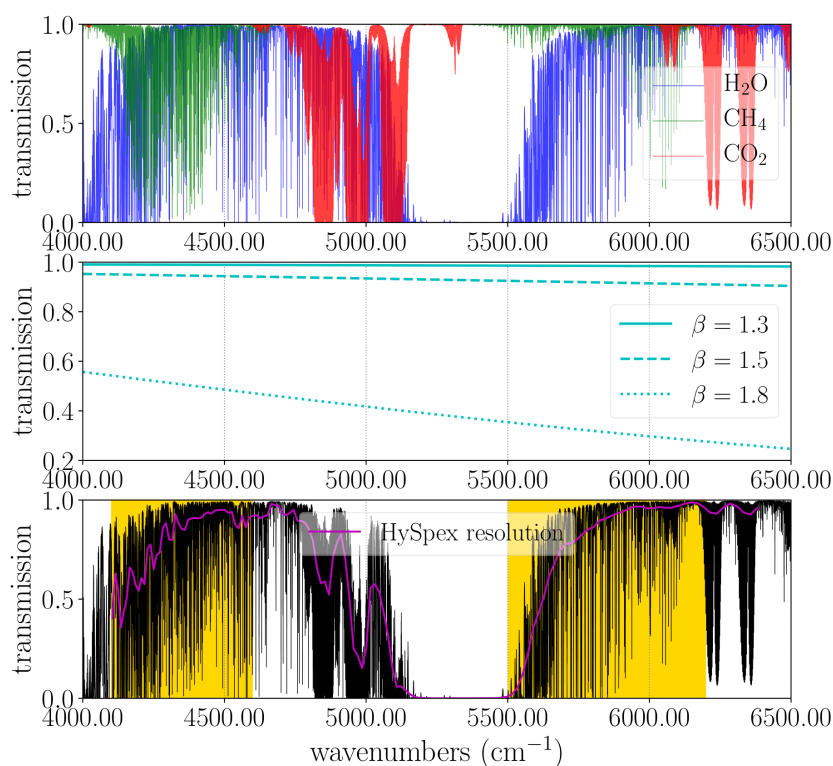


**Figure 4.** Monochromatic transmissions of CH<sub>4</sub>, CO<sub>2</sub> and H<sub>2</sub>O for the SWIR spectral range and a nadir looking observer at 1.5 km at a solar zenith angle (SZA) of 30° are depicted in the top panel. The aerosol transmission in the middle panel shows only smooth variations across the spectrum. The magenta line in the lower panel represents the total transmission degraded to HySpex resolution and the spectral intervals with methane absorption are indicated by the yellow background. Also note significant differences in transmissions of the monochromatic spectrum and convolved instrument spectrum.

The molecular absorption calculations in this study exploit GEISA (Gestion et Etude des Informations Spectroscopiques Atmosphériques; Delahaye et al., 2021) 2020 spectroscopic line data. In the top panel of Fig. 4 the individual components of the monochromatic total transmission for the US-Standard atmosphere are shown. Methane's first overtone of the fundamental vibrational transition  $2\nu_3$  (with its P and R branches) is found around  $6000\text{ cm}^{-1}$  while additional (strong) absorption lines range from  $4100\text{--}4700\text{ cm}^{-1}$  (band center  $\approx 4420\text{ cm}^{-1}$ ). The panel at the bottom demonstrates how the total monochromatic transmission (in black) is smoothed by the observer's coarse spectral resolution.

In Fig. 5 the BIRRA Jacobian matrix for two spectral intervals with strong methane absorption is depicted, respectively.

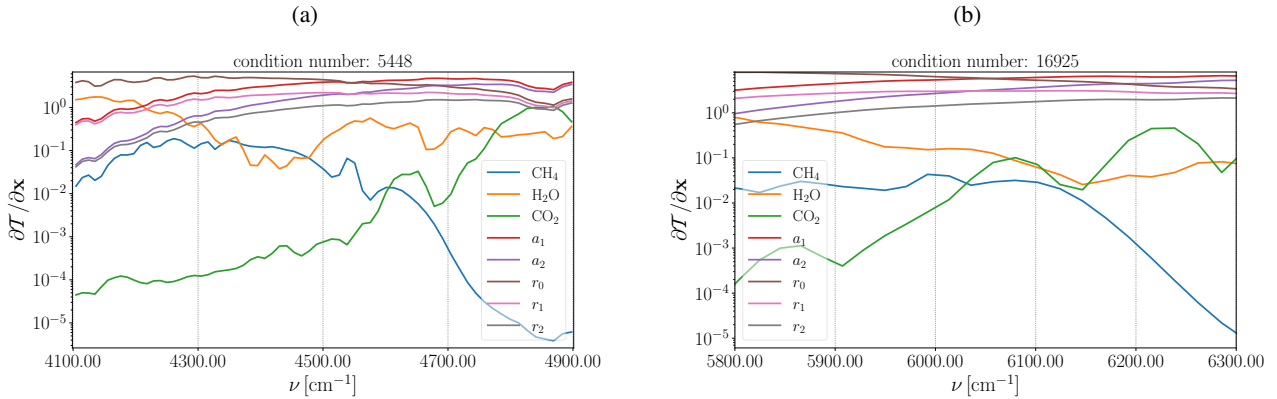


**Figure 5.** Columns of the Jacobian matrix and condition numbers in the 4100–4900 cm<sup>-1</sup> (left) and 5800–6300 cm<sup>-1</sup> (right) spectral intervals.

#### 195 2.4.1 Nonlinear least squares solvers

Various nonlinear retrieval schemes were examined and are briefly introduced subsequently. The iterative nature of nonlinear least squares methods requires the calculation of derivatives for each of the nonlinear state vector elements across the spectral axis which is represented by the Jacobian matrix  $J$ . The feasibility of a given retrieval setup is briefly studied after the introduction of the various solvers in Sec. 3.1.1. Therefore the condition number of the Jacobians are examined for different spectral intervals relevant for the SWIR CH<sub>4</sub> retrieval.

The retrieval's performance, e. g., the fit quality, is assessed with respect to the 2-norm of the discrepancy between the measurement  $\mathbf{y}$  and the converged spectrum  $\sigma = \|\mathbf{y} - \mathbf{I}(\mathbf{x})\|_2$ , also known as the residual norm. The least squares (error) covariance matrix is given by

$$\Xi = \frac{\sigma^2}{(m - n)} (\mathbf{J}^T \mathbf{J})^{-1} \quad (8)$$

where  $J$  represents the Jacobi matrix, while  $m$  and  $n$  specify the number of measurements and number of state vector elements, respectively. The errors of the individual state vector parameters are obtained from the diagonal elements of  $\Xi$ .

#### Nonlinear least squares (NLS)

The nonlinear least squares fit minimizes the objective function  $\mathcal{L}$  for given measurements  $\mathbf{y}$  according to

$$\min_x \{\mathcal{L}(\mathbf{x})\} = \min_x \|\mathbf{y} - \Phi(\mathbf{x})\|_2^2, \quad (9)$$

and applies when the model function  $\Phi$  is nonlinear in one or more parameters of  $\mathbf{x}$ .



### Separable least squares (SLS)

The so called separable least squares solver splits (separates) the state vector  $\mathbf{x}$  into nonlinear and linear parameters  $\mathbf{x} = (\boldsymbol{\eta}, \boldsymbol{\beta})$  where the elements in  $\boldsymbol{\beta}$  enter the forward model  $\Phi$  linearly (see Sec. 2.5) while the components in  $\boldsymbol{\eta}$  are of nonlinear nature. The minimization problem is hence given by

$$215 \quad \min_{\boldsymbol{\eta}, \boldsymbol{\beta}} \|\mathbf{y} - \Phi(\boldsymbol{\eta}) \boldsymbol{\beta}(\boldsymbol{\eta})\|_2^2. \quad (10)$$

This setup is also known as the Variable Projection (VarPro, Golub and Pereyra, 2003) method where  $\boldsymbol{\eta}$  is independent of  $\boldsymbol{\beta}$  in the matrix product  $\Phi(\boldsymbol{\eta}) \boldsymbol{\beta}(\boldsymbol{\eta})$ . The parameters in  $\boldsymbol{\eta}$  can hence be fitted in the usual way by means of Gauss–Newton or Levenberg–Marquardt algorithms (see e. g. Hansen et al. (2013)).

### Generalized least squares (GLS)

220 A so called generalized least squares fit can be employed to account for correlated errors. The covariance matrix  $\mathbf{C}$  is used to account for the spectral variations of the scene’s background, i. e. parts of the flight track which are presumably not influenced by the  $\text{CH}_4$  plume. Therefore, the location of the point source along with wind data needs to be known. The matrix  $\mathbf{C}$  is then created by computing the spectral covariance for a given scene. The idea is that possible background variations similar to the methane band absorption are not (mistakenly) interpreted as a molecular enhancement. The covariance matrices for the  
225 methane retrieval intervals are depicted in Fig. 6.

The symmetric positive semidefinite error covariance matrix  $\mathbf{C}$  is (pre-)computed for a given flight track so that the non-negative square root matrix  $\mathbf{S} = \mathbf{C}^{\frac{1}{2}}$  can be used to estimate  $\mathbf{x}$  according to

$$\min_{\mathbf{x}} \|\mathbf{S}^{-1}(\hat{\mathbf{y}} - \mathbf{J}\mathbf{x})\|_2^2. \quad (11)$$

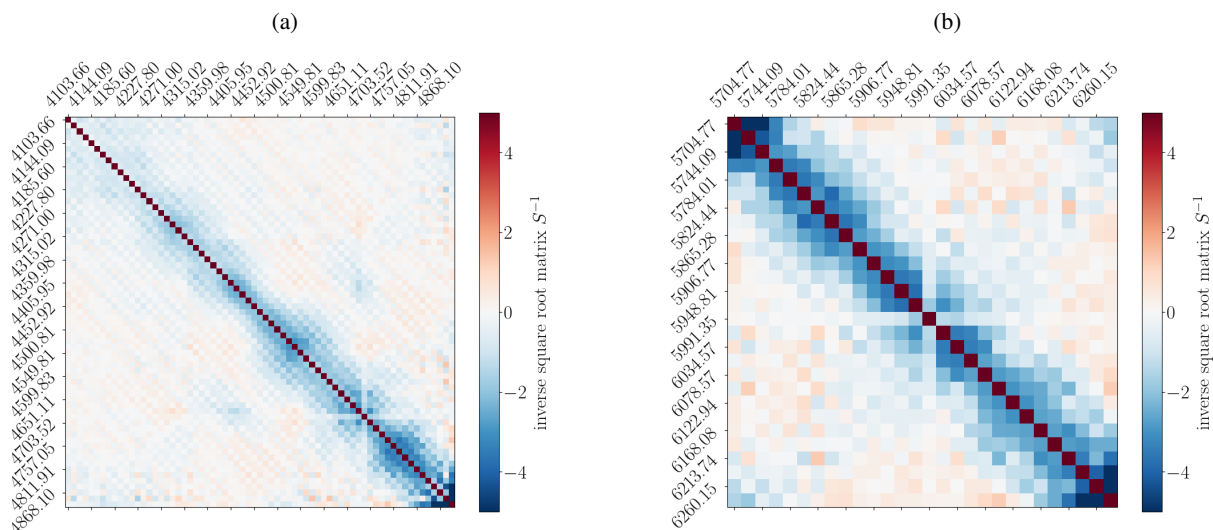


**Figure 6.** Scene 09 background covariance matrix  $S$  for the (a) 4100–4900  $\text{cm}^{-1}$  (left) and (b) 5700–6300  $\text{cm}^{-1}$  (right) spectral range. Note that beside the bad HySpex pixel mentioned in Fig. 2 at 5992.74  $\text{cm}^{-1}$  there appears to be another suspect pixel at 4691.04  $\text{cm}^{-1}$ .

## 2.4.2 Methane enhancement estimate

230 In order to estimate the  $\text{CH}_4$  plume enhancement light path modifications and the retrieval’s vertical sensitivity need to be taken into account. A ‘scene average’  $\text{CO}_2$  scaling factor is used to correct for light path modifications (Frankenberg et al., 2005; Schneising et al., 2009; Krings et al., 2011; Borchardt et al., 2021). In order to apply the  $\alpha_{\text{CO}_2}$  scaling factor to  $\text{CH}_4$  enhancements for the correction of light path modifications below instrument altitude, the different concentration profiles of  $\text{CH}_4$  and  $\text{CO}_2$  (see Fig. 3) need to be taken into account hence  $\tilde{\alpha}_{\text{CO}_2}$  is introduced. The ‘scene averaging’ method was also

235 applied to infer the actual  $\text{CH}_4$  background profile for the respective overpass. It is important to note that for the  $\text{CO}_2$  and  $\text{CH}_4$  background fits ground pixels around the suspected  $\text{CH}_4$  sources were excluded when computing the average spectrum. The lack of vertical atmospheric resolution in the observed spectrum requires the application of averaging kernels in order to account for the retrieval’s altitude sensitivity. The column averaging kernel  $\kappa_m(z)$  is used to describe the sensitivity of the total columns to changes in molecular concentrations at different levels (see Buchwitz et al., 2004).

240 The actual  $\text{CH}_4$  column, which includes corrections for light path modifications via  $\tilde{\alpha}_{\text{CO}_2}$  and accounts for the retrieval’s vertical sensitivity with respect to the target by  $\kappa_{\text{CH}_4}(z)$ , is finally computed as the sum of the background and plume component according to

$$N_{\text{CH}_4} = N_{\text{bg}} + \frac{\alpha_{\text{CH}_4}}{\tilde{\alpha}_{\text{CO}_2}} \hat{N}_{\text{pl}}(z_0), \quad (12)$$



with

$$245 \quad \hat{N}_{\text{pl}}(z_0) = \int_{z_0}^{z_{\text{pl}}} \frac{n_{\text{pl}}(z)}{\kappa_{\text{CH}_4}(z)} dz. \quad (13)$$

The (highly variable) water vapor concentration is co-retrieved with the  $\text{CH}_4$  plume enhancements as results indicate degeneracy between  $\text{H}_2\text{O}$  and the reflectivity polynomial so that the  $\text{H}_2\text{O}$  scaling factor and reflectivity coefficients need to be interpreted as ‘effective’ parameters that capture low frequency components in the spectrum. The ‘mixing’ of usually clearly separated spectral features is attributed to the coarse spectral resolution of HySpex measurements and the fact that water vapor  
 250 absorption lines of similar strength are distributed over a wide spectral range.

## 2.5 Linear fitting algorithms

### Linear least squares (LLS)

Linearization of the BIRRA forward model with respect to  $\alpha_{\text{CH}_4}$  allows to infer methane enhancements by linear least squares. In analogy to Thompson et al. (2015, Sec. 2.4) where the  $\text{CH}_4$  enhancement is estimated from the linear scaling of a target  
 255 signature that perturbs the mean radiance, linearization of Beer’s law caused by an increase in methane’s total optical depth in the lowest part of the atmosphere ( $< 2$  km) with respect to the (saturated, see Thompson et al. (2015)) background concentration is justified.

In order to estimate the unknown parameters in  $\mathbf{x}$  by linear least squares the power-series expansion for the exponential function  $\exp(\tau) := \sum_{n=0}^{\infty} \frac{\tau^n}{n!}$  is exploited. Assuming that the increased optical depth caused by the plume  $\tau_{\text{plume}}$  is rather  
 260 small the Taylor expanded transmission spectrum for the plume can be approximated as

$$\exp\left(-\tau_{\text{plume}}^{\downarrow\uparrow}(\nu)\right) \approx \left(1 - \beta_{\text{CH}_4} \tau_{\text{plume}}^{\downarrow\uparrow}(\nu)\right). \quad (14)$$

The forward model for the linear least squares problem of  $M$  measurements can then be formulated according to

$$\{\Phi(\mathbf{x})\}_i = \sum_{j=1}^N x_j \phi_j(\nu_i), \quad i = 1, 2, \dots, M \quad (15)$$

so that the model functions for the linear parameters of the state vector  $\mathbf{x} = (r_0, b_0 = r_0 \beta_{\text{CH}_4})$  are given by

$$265 \quad \phi_1 = \frac{\cos(\theta)}{\pi} I_{\text{sun}} \mathcal{T}^{\downarrow\uparrow} \otimes S,$$

$$\phi_2 = -\frac{\cos(\theta)}{\pi} I_{\text{sun}} \mathcal{T}^{\downarrow\uparrow} \tau_{\text{plume}}^{\downarrow\uparrow} \otimes S.$$

Note that the reflectivity coefficient  $r_0$  is present in both elements of  $\mathbf{x}$ . However, this should not pose a problem for the linear fit as the model functions are different. A brief analysis on the condition of  $\Phi(\mathbf{x})$  in the  $5700\text{--}6300\text{ cm}^{-1}$  interval revealed a condition number is 885. When the higher order reflectivity coefficient  $r_1$  is included the number increases by one order of  
 270 magnitude and another order if  $r_2$  added. Therefore, in the current setup, the linear fit is only feasible for the estimate of  $r_0$  and  $\beta_{\text{CH}_4}$  at the same time. However, using standardized radiances by dividing by a fitted polynomial eliminates the need for higher order reflectivity coefficients even for large intervals.



### 2.5.1 Matched Filter (MF)

A well established method to estimate molecular concentration enhancements from hyperspectral sensors is the MF (Theiler  
 275 and Foy, 2006; Villeneuve et al., 1999; Funk et al., 2001; Thompson et al., 2015). The linear enhancement factor estimate is  
 based on the perturbation of an average (background) radiance spectrum  $\mu$  by a known target spectrum  $t$  and is formulated  
 according to

$$\beta(\mathbf{y}) = \frac{(\mathbf{J} - \mu)^T \mathbf{C}^{-1} (\mathbf{y} - \mu)}{\sqrt{(\mathbf{J} - \mu)^T \mathbf{C}^{-1} (\mathbf{J} - \mu)}}. \quad (16)$$

The method tests an observed vector  $\mathbf{y}$  against a base vector represented by e. g. the  $\text{CH}_4$  plume Jacobian  $\mathbf{J}$  (computed with a  
 280 radiative transfer model, e. g., Py4CAtS) while accounting for the background covariance  $\mathbf{C}$ . The method also assumes that the  
 measured spectrum can be represented as a linear superposition of the plumes optical depth and the mean radiance  $\mu$  according  
 to

$$\mathbf{y} \approx \mathbf{I} = \mu(1 - \tau_{\text{pl}}^{\downarrow\uparrow})\beta. \quad (17)$$

In order to allow for a comparison to the BIRRA setups, the target's signature  $\tau_{\text{pl}}^{\downarrow\uparrow}$  represents the vector of optical depth for a  
 285 low level plume ( $< 2$  km with 390 ppm  $\text{CH}_4$ ) that is scaled by the linear enhancement factor  $\beta$  that perturbs the mean radiance.  
 Note that the mean background spectrum  $\mu$  and  $\mathbf{C}$  were computed per scene and the inverse covariance  $\mathbf{C}^{-1}$  is approximated  
 by decomposing  $\mathbf{C}$  into eigenvalues and eigenvectors (Thompson et al., 2015, Eq. 6-8).

As pointed out by Guanter et al. (2021) the classical matched filter is relatively sensitive to surface albedo hence also the  
 cluster tuned matched filter (Funk et al., 2001) was examined. Classification of the image reduces the within-class variance  
 290 which in turn should reduce the albedo sensitivity of  $\beta$ . So instead of computing a single covariance (background) statistic  
 the cluster tuned matched filter computes background statistics  $\mathbf{C}_i$  for each cluster  $i$  determined by k-means (Thorpe et al.,  
 2013; Nesme et al., 2020). The elbow method (Thorndike, 1953) was employed to estimate the suitable number of clusters for  
 a scene.

### 2.5.2 Singular Value Decomposition (SVD)

The retrieval of methane enhancements from hyperspectral AVIRIS data using singular vectors of the observed spectrum plus  
 295 a target signature was first demonstrated by Thorpe et al. (2014). In this study the uncorrelated (orthogonal) singular vectors  
 are obtained from HySpex spectra within a scene (flight track) that are (assumed to be) not impacted by the plume. The scene's  
 mean standardized background spectrum was decomposed while the target spectrum represented by the  $\text{CH}_4$  plume's Jacobian  
 given by

$$\mathbf{t} = -\mu \exp(-\tau_{\text{CH}_4})\tau_{\text{pl}} \quad \text{with} \quad \tau_{\text{CH}_4} = \tau_{\text{bg}} + \beta\tau_{\text{pl}} \quad (18)$$

was computed with the radiative transfer code Py4CAtS. Note that  $\tau_{\text{bg}}$  represents methane's background optical depth for the  
 lowest, plume impacted layers.

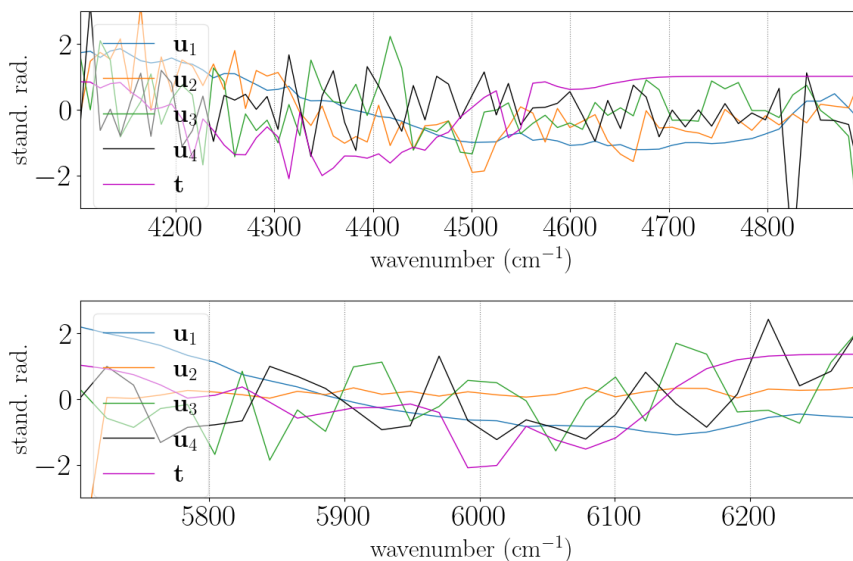


**Figure 7.** The first four singular vectors after standardization, i. e., removing the mean and scaling to unit variance, along with the methane plume’s target signature  $t$ .

The basic idea corresponds to the MF, i. e., to represent the general variability in spectral radiance by a linear combination of singular vectors and a target signal. The minimization problem is then given by

$$\min_w \|y - Aw\|_2^2 \quad \text{with} \quad (19)$$

$$Aw = \sum_k^N u_k w_k + t w_{\text{CH}_4} \quad (20)$$

where  $A$  represents the concatenated matrix of the first  $N$  columns of the unitary matrix  $U$  and the vector  $w$  contains the corresponding weights. The contribution of enhanced methane in the lowest atmospheric layers to the measured radiance is estimated by the corresponding weight of the  $\text{CH}_4$  target signature.

310 It was found that  $N = 4$  is a good choice across spectral intervals as including additional columns significantly increased the condition number of  $A$ . It should be noted that cluster tuning was also examined for the SVD fits. In this case the background spectra were clustered by k-means and the SVD performed for each cluster separately and the respective base vectors per cluster were then used in the linear fit.

### 2.5.3 Spectral signature detection (SSD)

315 A very simple yet effective method to detect elevated concentrations of methane in a flight track (subsequently designated as a ‘scene’) is based on the ratio of spectral residual norms. This method does not require any radiative transfer calculations, look up tables or initial guess information but only calibrated (digital numbers are sufficient) sensor data for a given interval.





320 The algorithm is based on a simple polynomial fit of spectral pixels and the computation of spectral residuals. The idea of the method is similar to the continuum interpolated band ratio (CIBR) Green et al. (1989) and Thompson et al. (2015, Eq. 2) which also scores absorption depths (Pandya et al., 2021).

The application of our signature detection method requires the spectral interval including  $m$  pixels to be separated into section(s) where  $\text{CH}_4$  absorbs and where it does not (or only weakly). The detection method then applies a linear least squares to fit a polynomial of some degree  $P$  to  $Q$  out-band pixels

$$p(\beta, \nu_i) = \sum_{j=0}^P \beta_j \nu_i^j, \quad i = 1, 2, \dots, Q. \quad (21)$$

325 Next the residual norms

$$r = \|\mathbf{y} - \mathbf{p}\|_2^2. \quad (22)$$

for the out-band pixels and  $(M - Q)$  in-band-pixels are computed so that their ratio

$$s = \frac{r_{\text{in}}}{r_{\text{out}}} \quad (23)$$

330 yields an absorption band depth score for each observation. Variations in the score indicate variations in the  $\text{CH}_4$  absorption. If a constant (zero order polynomial) is used for the out-band fit, the method is similar to the CIBR algorithm. With higher order polynomials the wavenumber dependent contributions from the surface reflectivity and other known interfering species could be modeled more accurately, particularly over larger intervals.

The algorithm constitutes a fast detection scheme which can also be applied for real-time detection of enhancements, e. g., determine whether or not a  $\text{CH}_4$  ventilation shaft is active at the time of instrument overpass.

### 335 3 Results

In this section the results of the prescribed retrieval methods are presented based on HySpex nadir observations in the short-wave infrared. The section starts with a feasibility study for different BIRRA setups. The results focus on HySpex measurements from flight track 9 (scene 9) since it was found to be the one with the strongest emission at the time of overpass so that the results of the various retrieval schemes can be compared. Note that this ventilation shaft was actually overpassed two times, 340 i. e., in flight tracks 9 and 11 from aircraft altitude  $\approx 1520$  m and  $\approx 2900$  m, respectively. This circumstance could e. g. be used to study the impact of spatial resolution on concentration enhancements.

#### 3.1 Beer InfraRed Retrieval Algorithm

The section begins with a feasibility assessment for different BIRRA state vectors and presents the retrieval results from HySpex measurements using the retrieval's NLS, SLS and GLS setups.



### 345 3.1.1 Feasibility of BIRRA state vectors

According to Table 1 the reduced parameter space in the separated least squares improves the condition number of its Jacobian. The assessment also revealed that increasing the spectral resolution by a factor of two improves the condition number by  $\approx 10\%$  meaning that the condition number in Fig. 5 would be  $\approx 30\%$  lower if HySpex would measure at a resolution of  $0.2\text{--}0.3\text{ cm}^{-1}$  FWHM.

**Table 1.** Condition numbers for the Jacobian matrices of various state vectors of the intervals  $4100\text{--}4900\text{ cm}^{-1}$  (designated as 4K) and  $5700\text{--}6300\text{ cm}^{-1}$  (6K), respectively. The upper part of the table shows the condition numbers for the nonlinear fit while the lower part gives the conditions for the Jacobians only containing the nonlinear parameters (required for the VarPro solver). The state vector component  $N_m = 3$  represent the three molecular scaling factors ( $\alpha_{\text{CH}_4}$ ,  $\alpha_{\text{H}_2\text{O}}$ ,  $\alpha_{\text{CO}_2}$ ),  $N_a$  stands for the aerosol scaling factors (e. g.,  $a_1$ ,  $a_2$ ), and  $N_r$  represents the number of coefficients (e. g.,  $r_0, r_1, r_2$ ) of the reflectivity polynomial.

$x$	$4100\text{--}4900\text{ cm}^{-1}$ (4K)	$5700\text{--}6300\text{ cm}^{-1}$ (6K)	combined
$N_m = 3, N_r = 3, N_a = 0$	189	1323	147
$N_m = 3, N_r = 3, N_a = 1$	730	2269	187
$N_m = 3, N_r = 3, N_a = 2$	6681	50625	198
$\eta$	$4100\text{--}4900\text{ cm}^{-1}$ (4K)	$5700\text{--}6300\text{ cm}^{-1}$ (6K)	-
$N_m = 3$	9	32	-
$N_m = 3, N_a = 1$	47	499	-
$N_m = 3, N_a = 2$	88	839	-

### 350 3.1.2 Nonlinear least squares

The state vector  $x = (3m, 3r)$  was found to be robust toward low SNR values across the examined spectral intervals and is hence the first choice for the subsequent retrievals. However, because  $\text{CO}_2$  is required to account for light path modifications, the actual retrieval fits the state vector  $x = (\alpha_{\text{CH}_4}, \alpha_{\text{H}_2\text{O}}, 3r)$ . The scene averaged  $\text{CO}_2$  background level is inferred from the  $1.6\text{ }\mu\text{m}$  and/or  $2\text{ }\mu\text{m}$  bands via the multi-interval fit. The decision to exclude aerosol parameters from the  $\text{CH}_4$  plume fit was also encouraged by findings from Borchardt et al. (2021), as they conclude that different aerosol scenarios in the SWIR do not induce errors  $> 0.2\%$ . Moreover, since the spectra are observed at low flight altitudes (between 1500 m and 3000 m above mean sea level (MSL)) on a clear day (Luther et al., 2019) retrieval errors induced by aerosol scattering should be negligible in our scenario too (also see Fig. 4) (Thorpe et al., 2013; Thompson et al., 2015). Nonetheless, aerosol extinction according to Eq. (2) could still be included as a given input argument in the forward model.

360 The  $\text{CO}_2$  was found to be 385–400 ppm for scene 09 and 365–380 ppm for scene 11 depending on the spectral interval. Given twice the instrument altitude for scene 11 the relative difference of the retrieved values for both scenes is reasonable as changes in  $\text{CO}_2$  are attributed to light path modifications (light path shortening due to single scattering). The average difference of 20 ppm motivated the choice of a scaling factor  $\tilde{\alpha}_{\text{CO}_2} = 0.96$  for scene 09 and  $\tilde{\alpha}_{\text{CO}_2} = 0.93$  for scene 11. The scene averaged



CH<sub>4</sub> background profile was also determined in advance and found to be within 5 % of the initial guess of 1850 ppb so that its  
365 initial guess was not scaled.

In Figs. 8a and 8b the results for the retrieval from  $3 \times 3$  averaged observations for scene 09 from 4150–4900 cm<sup>-1</sup> (4K)  
and 5700–6300 cm<sup>-1</sup> (6K) are shown, respectively. Averaging over multiple HySpex observations is a way to increase SNR  
and reduces scattering of the inferred quantities. In both spectral intervals a CH<sub>4</sub> enhancement is identified and both reveal  
significant levels of CH<sub>4</sub> (up to  $\approx 4000$  ppb) at and close to the source (ventilation shaft). Furthermore, the results agree on  
370 the direction of advection. Interestingly the surface-type dependent bias is opposite in the 4K and 6K intervals. The issue of  
different surfaces types and their impact on the uncertainty of CH<sub>4</sub> quantification for moderately resolved spectra was also  
described by Borchardt et al. (2021) who observed similar features, i. e., paved concrete induces a positive bias while barbed  
goatgrass leads to large underestimation of enhancements (and so the total column) as at rather coarse spectral resolutions the  
reflected spectrum shows interfering features similar to the absorption of CH<sub>4</sub>.

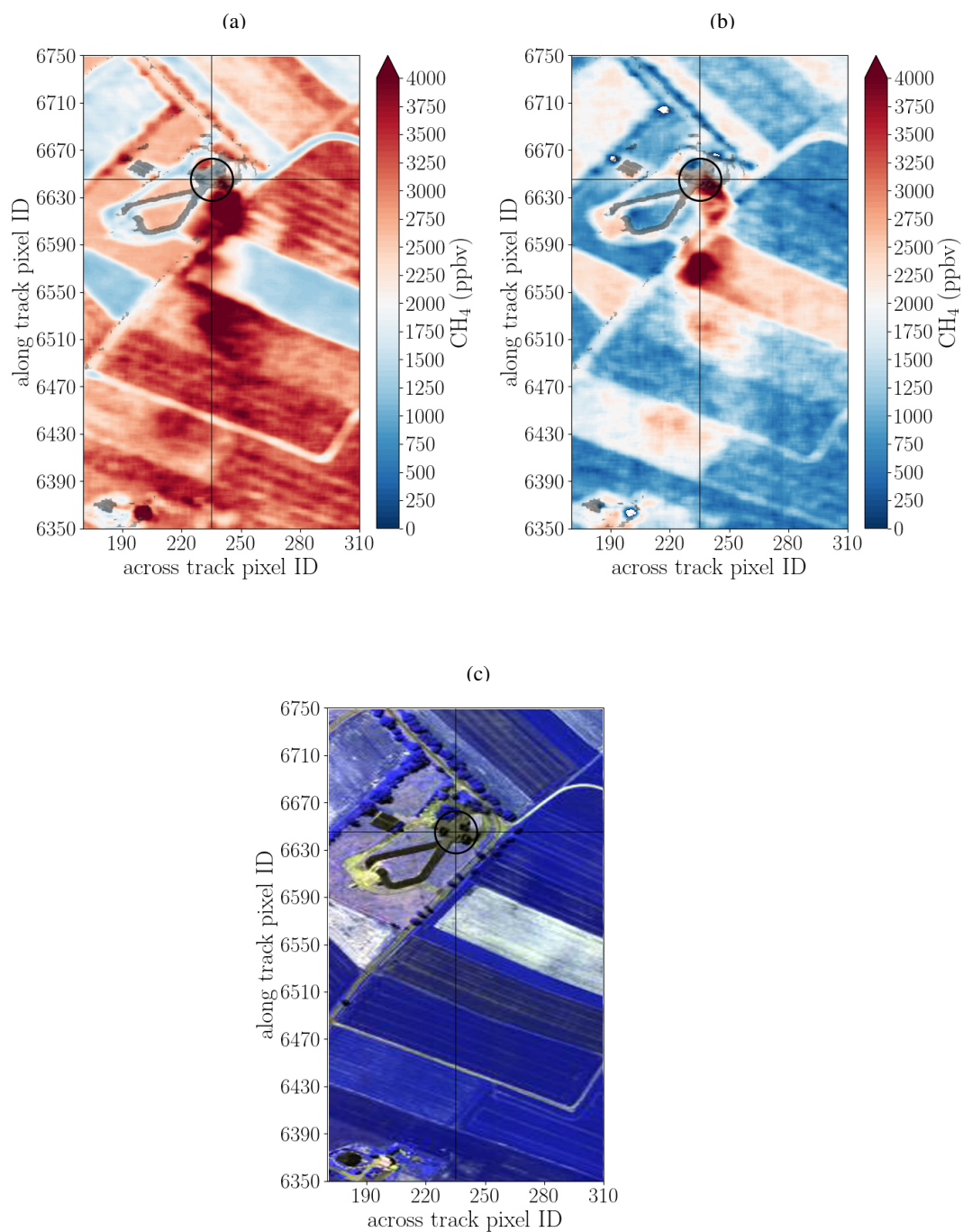


**Figure 8.** Retrieved CH<sub>4</sub> enhancement of  $3 \times 3$  spatially averaged HySpex observations in the (a)  $4150\text{--}4900\text{cm}^{-1}$  (4K) range and (b)  $5700\text{--}6300\text{cm}^{-1}$  (6K) range. Interestingly, the albedo related biases show an almost identical pattern but reverse sign. (c) False color image of the SWIR-320m-e camera around the Pniovek V shaft in scene 09.



375 In spite of a significantly stronger signal in the 6K range (see Fig. 2), the significantly higher condition number of its Jacobians (see Table 5) make both intervals similarly suitable for the retrieval of methane.

With this finding the multi-interval retrieval, i. e., combining 4K and 6K ranges, is expected to yield better results given that methane is fitted across intervals so that the additional constraint alleviates albedo induced variabilities on the target. Figure 9 depicts the inferred  $\text{CH}_4$  enhancements for scene 09 with the multi-interval retrieval. The surface correlated bias is still present  
380 but reduced compared to the single-interval fits. The maximum enhancements and pattern of the  $\text{CH}_4$  plume is similar but the downwind shape of the plume is better captured.

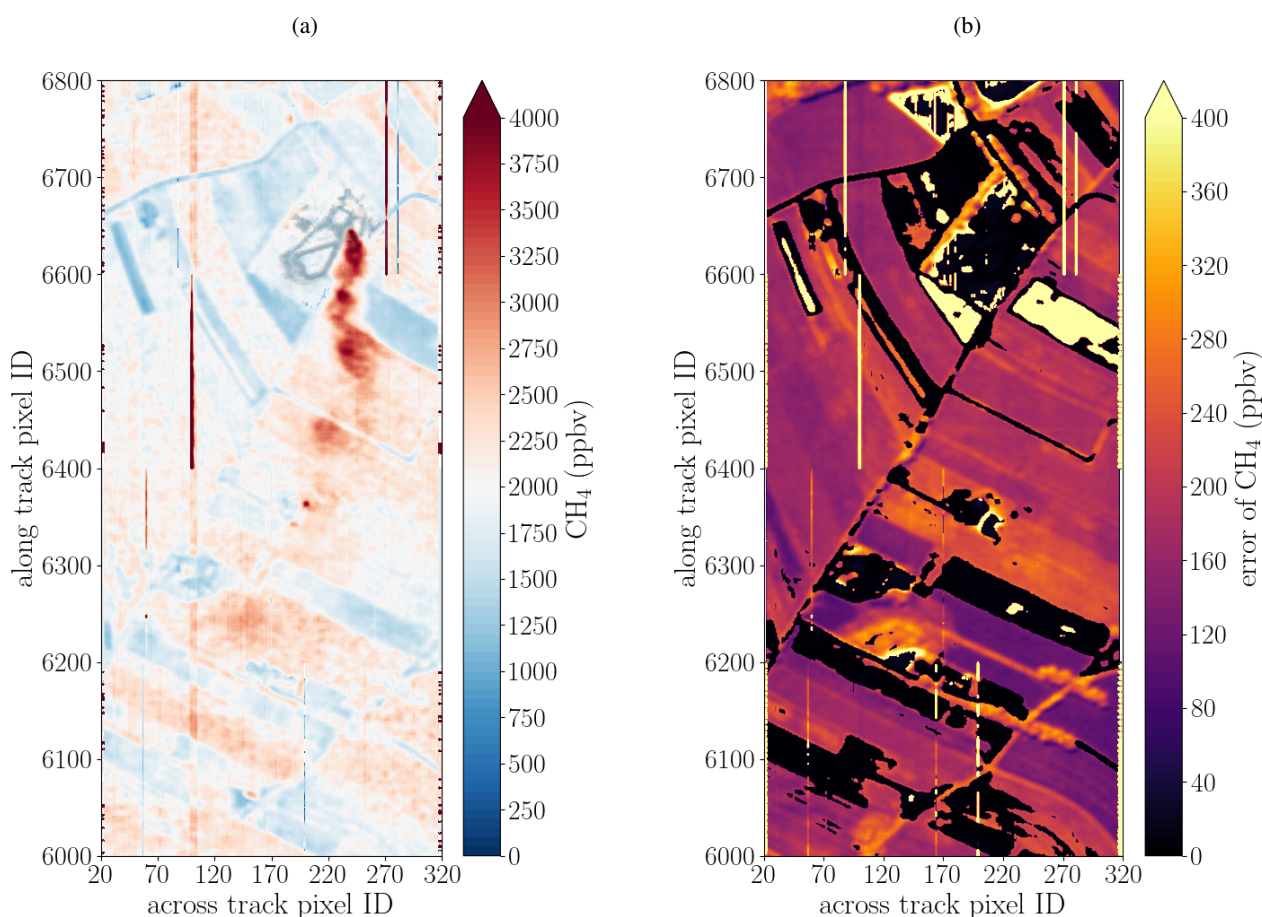


**Figure 9.** (a) Methane plume with corresponding errors in (b) inferred for  $3 \times 3$  spatially averaged HySpex observations with the multi-interval fit for the combined intervals  $4150\text{--}4900\text{ cm}^{-1}$  and  $5700\text{--}6300\text{ cm}^{-1}$ . The fitted state vector was  $\boldsymbol{x} = (\alpha_{\text{CH}_4}, \alpha_{\text{H}_2\text{O}}, 6r)$ . The bluish colors correlate with either high or very low errors indicating observations with either a small albedo or reflectivity which could not be captured by the second order polynomial.





In another setup that in addition includes the aerosol parameter  $a_1$  similar  $\text{CH}_4$  concentrations were inferred. However, the  $a_1$  estimate adversely affects the fit of the reflectivity coefficients. The impact on  $r_0(6\text{K})$  was found to be stronger than on  $r_0(4\text{K})$ .

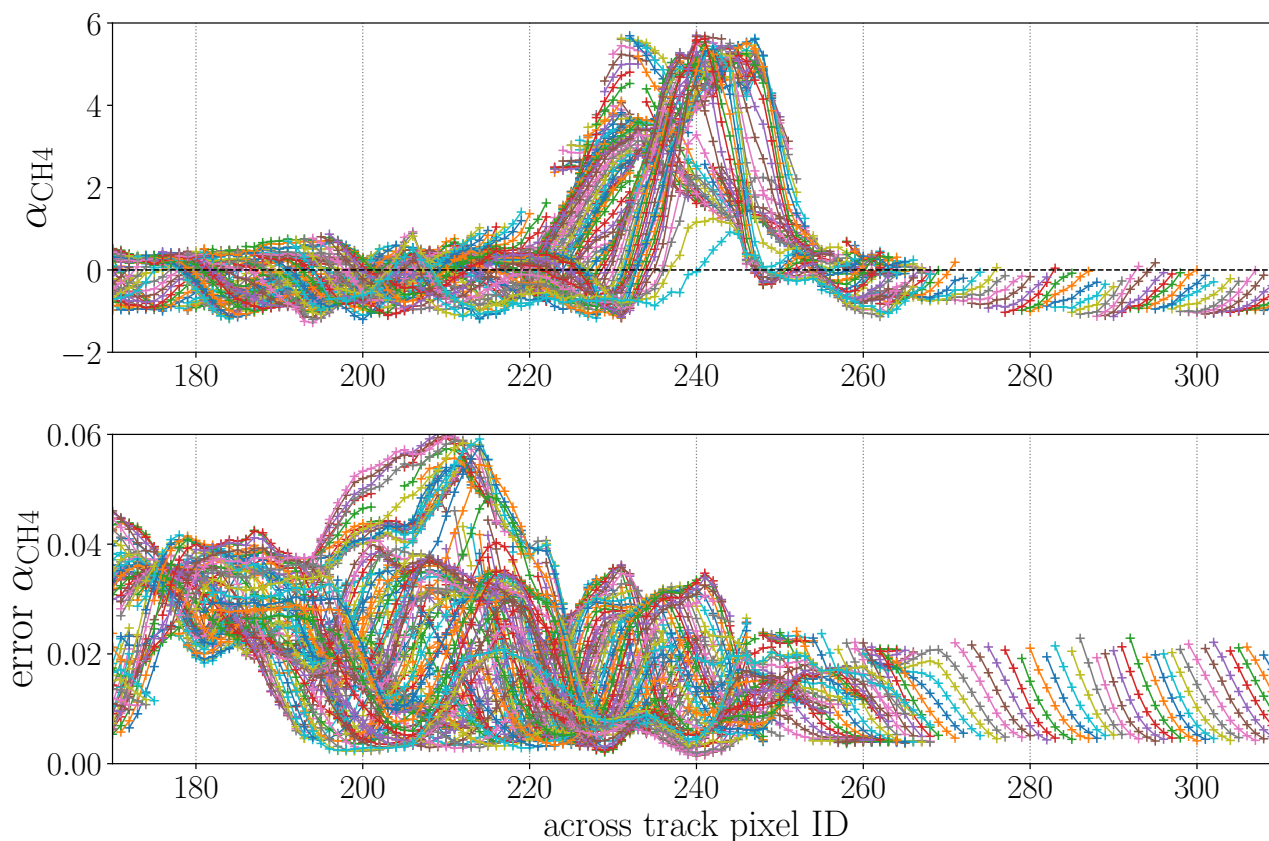


**Figure 10.** Across track depiction of the  $3 \times 3$  spatially averaged multi-interval fits from Fig. 9 for the along tracks pixels 6550–6650 are depicted. The top panel shows the corresponding  $\alpha_{\text{CH}_4}$  scaling factors while the errors are depicted in the lower panel. Note that filtering was applied for this figure.

385 The transverse section of the plume from Fig. 9 between along track pixels 6550–6650 is depicted in Fig. 10. This time the retrieval output was postprocessed so that outliers in the residual norms distribution and reflectivity coefficients  $r_0 > 1$  were filtered out. The output clearly identifies stable background  $\text{CH}_4$  concentrations and a significant enhancement between across track pixels 220–260 (two peaks). Variations in the plume’s shape further downwind from the source can also be studied. Note that a almost twofold increase methane’s total column corresponds to a  $\alpha_{\text{CH}_4} \approx 6$  (also see Sec. 3).



### 390 3.1.3 Separable least squares

The fit of single HySpex measurements with the separable least squares method turned out to be challenging as many retrievals did not converge due to the rank deficient linear problem. This confirms the findings from our simulations (not shown), which also indicate that the SLS algorithm is more sensitive to the quality of the spectra (SNR). In order to enhance the SNR of the measurements  $5 \times 5$  averages were used for the separable fits. The results for the SLS fit (VarPro) for the combined 4K and 6K intervals are depicted in Fig. 11. The retrieval output of the single window 4K and 6K retrieval mimic those of the NLS fit in Fig. 8.

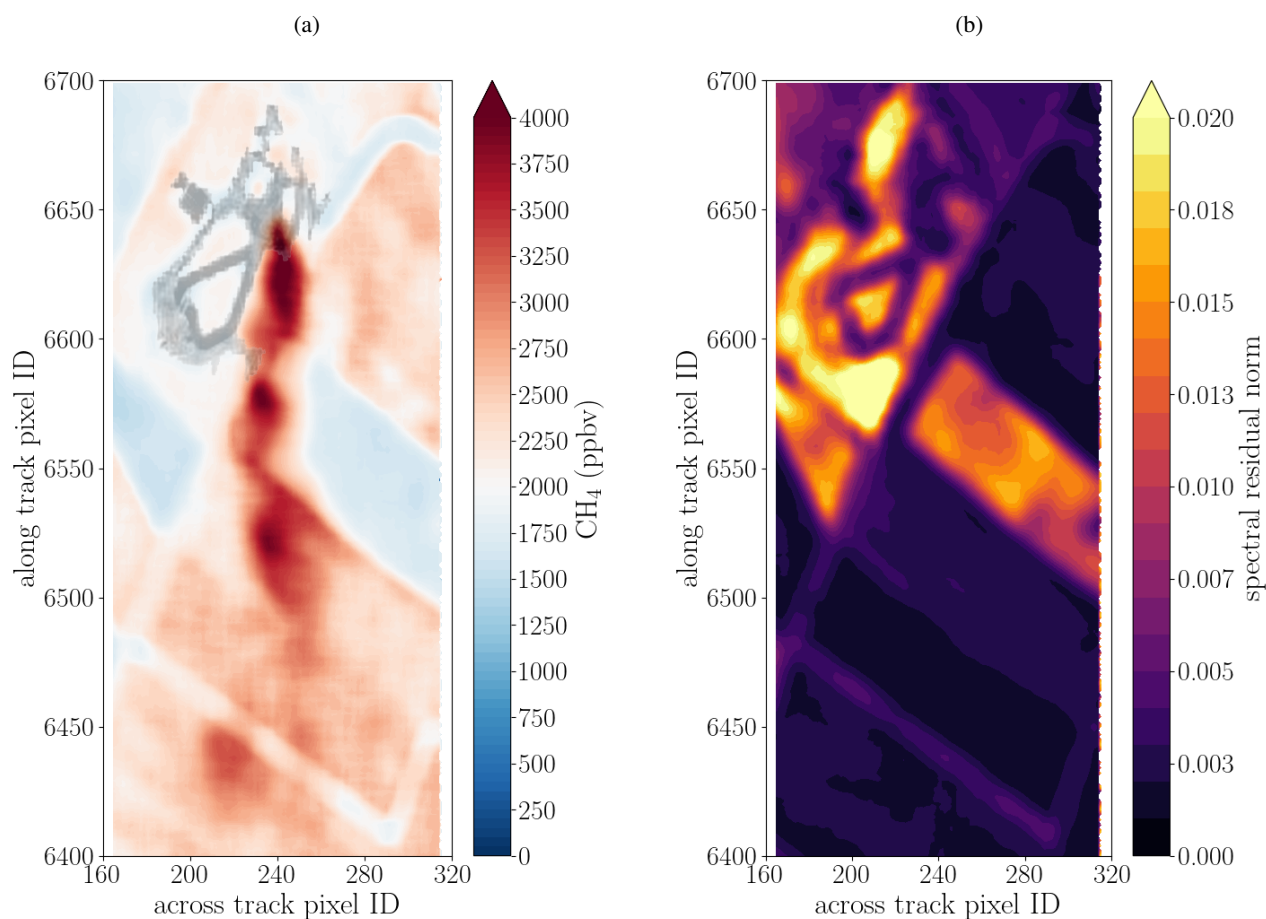


**Figure 11.** SLS fit for the combined 4K and 6K intervals for  $5 \times 5$  spatially averaged observations. (a) Methane plume enhancement and (b) corresponding spectral residual norms.





### 3.1.4 Generalized least squares

In Fig. 12 the retrieved columns for the generalized least squares (GLS) fit from  $3 \times 3$  averaged observations for scene 09 for the 4K and 6K intervals are shown, respectively. The algorithm employs the inverse of a scene's covariance structure to account for background statistics in the retrieval (Thorpe et al., 2013; Nesme et al., 2020) and is well suited for detecting concentrated sources. Correlation of methane enhancement and surface reflectivity is reduced yielding a more pronounced plume signal.

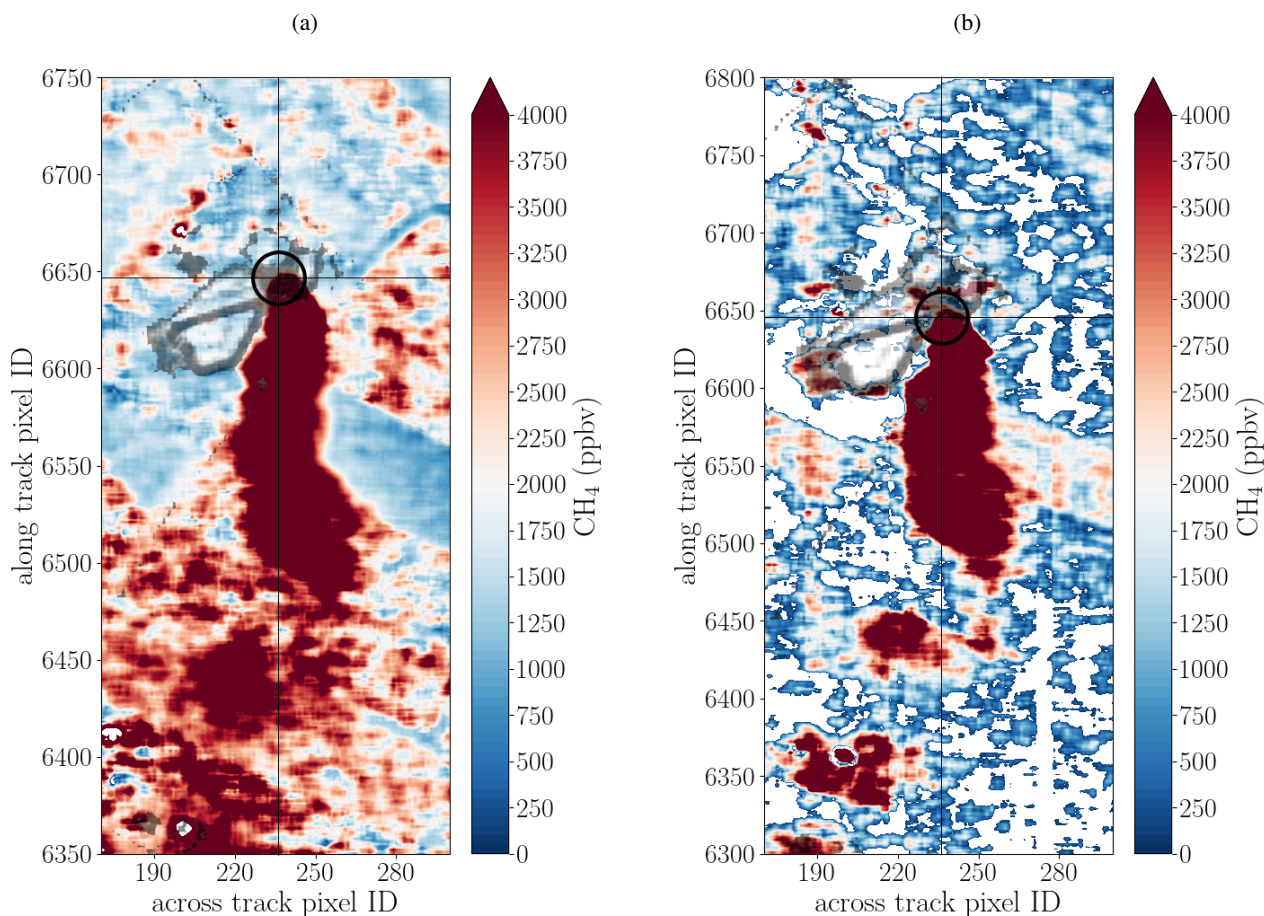


**Figure 12.** Methane plume for the GLS fit from (a)  $4150\text{--}4900\text{ cm}^{-1}$  and (b)  $5700\text{--}6300\text{ cm}^{-1}$  inferred for  $3 \times 3$  spatially averaged HySpex observations. White pixels did not converge and are therefore not included in the colorbar. The fitted state vector was  $\mathbf{x} = (\alpha_{\text{CH}_4}, 3r)$ .

### 3.1.5 LLS

Methane concentration enhancements can be inferred with the linear retrieval scheme given the state vector and retrieval interval are properly chosen. In Fig. 13a a small retrieval interval of  $\pm 50\text{ cm}^{-1}$  around  $6000\text{ cm}^{-1}$  with the state vector  $\mathbf{x} =$



405  $(r_0, b_0)$  was used. The small intervals also make the retrieval rather insensitive to variations in the ground albedo. Note that the  
 actual enhancement factor is found by dividing the first element of  $x$  by the second element, i. e.  $\beta_{\text{CH}_4} = b_0/r_0$  (see Sec. 2.5).  
 This setup was able to locate the source and also the drift of the  $\text{CH}_4$  plume with the wind is traceable several hundred  
 meters from the source. Also the enhancement factors agreed with the nonlinear fit within 20–50 % although the background  
 concentration appears to be negatively biased when compared with the nonlinear fit. The bias turned out to be sensitive to  
 410 the width of the spectral range and increased towards larger intervals while the fit quality decreased. Moreover, the fit was  
 only stable for small spectral intervals. More reflectivity coefficients have adverse impact on the fit as the problem becomes  
 very ill-conditioned. Using standardized radiances as pointed out in Sec. 2.5 eliminates the need for higher order reflectivity  
 coefficients in the linear fit and allows for larger spectral fit intervals.

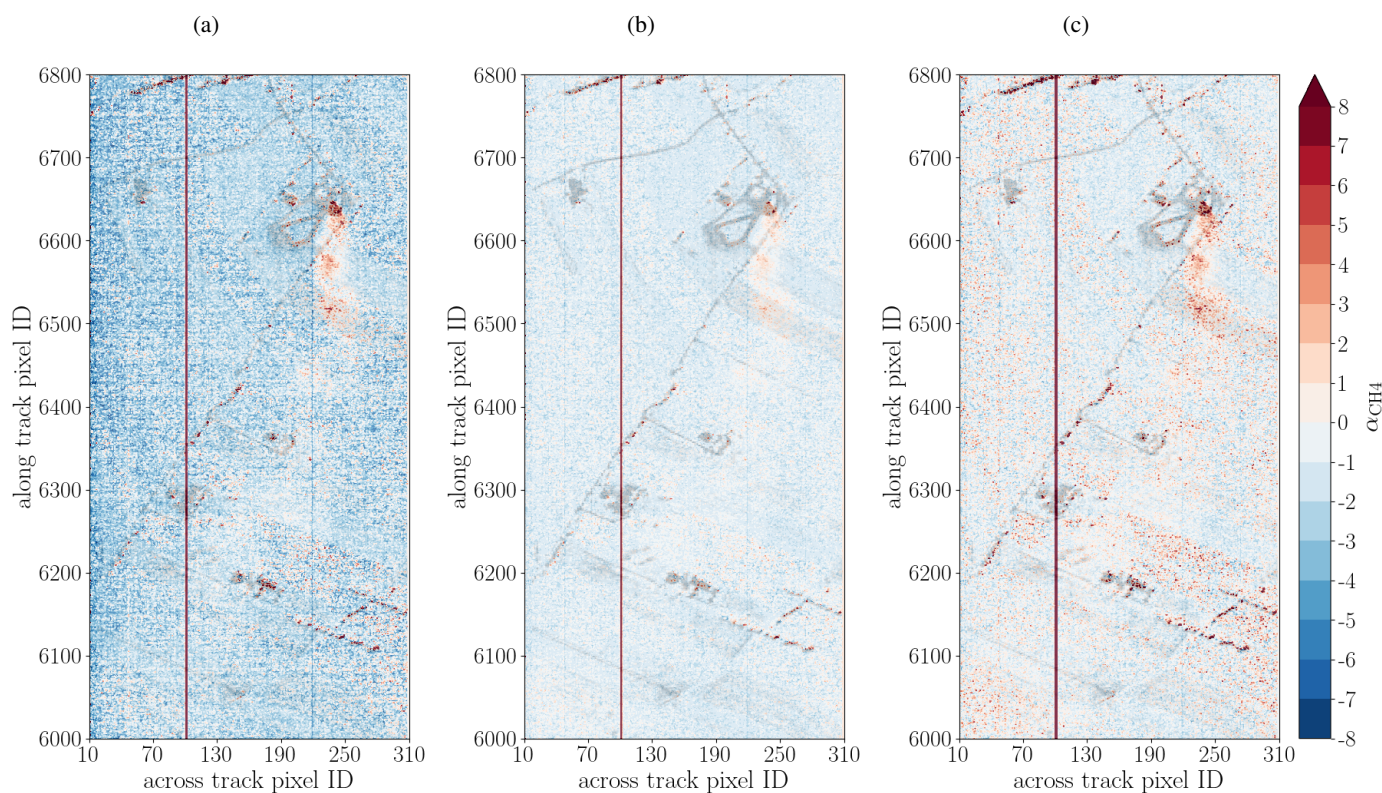


**Figure 13.** Retrieval of  $\text{CH}_4$  enhancements for individual HySpex observations from scene 09. Results in the first figure (a) shows the linear forward model setup with  $\mathbf{x} = (r_0, b_0)$  from  $5930\text{--}6080\text{ cm}^{-1}$  while (b) shows the subdivision setup  $\mathbf{x} = (r_0, r_1, r_2; \beta_{\text{CH}_4})$  from  $5900\text{--}6100\text{ cm}^{-1}$ . In the latter method the methane enhancements are less pronounced but the bias is also somewhat smaller. The NLS fit based on Eq. 6 for state vector  $\mathbf{x} = (r_0, r_1, r_2, \alpha_{\text{CH}_4})$  is depicted in (c). Note that the failed retrievals at across pixel ID 104 are caused by the pixel’s bad sensitivity at  $5992.74\text{ cm}^{-1}$  (see Fig. 2 and 6). It has significant impact on the fit since the selected retrieval interval for the linear fit is small and contains few pixels (see Fig. 2).



In order to facilitate larger retrieval intervals with higher order reflectivity polynomials a slightly modified linear retrieval  
415 setup was examined. It fits the reflectivity coefficients in the ‘wings’ of the retrieval window and subsequently estimates the  
enhancement factor  $\beta_{\text{CH}_4}$  in the interval between (the center region of the retrieval window)  $\mathbf{x} = (r_0, r_1, r_2; \beta_{\text{CH}_4})$ . The result  
is shown in Fig. 13b. The setup allows to increase the spectral interval and include additional coefficients in the state vector  
as the subdivision of the spectral interval avoids the attribution of variations in the  $\text{CH}_4$  absorption band to the reflectivity  
polynomial. However, it requires two linear least squares fits, i. e., one to estimate the reflectivity polynomial and another to  
420 fit  $\beta_{\text{CH}_4}$ . Note that the idea of separating pixels that belong to absorption and not was also employed in the in-band/out-band  
spectral residual fits in Sec. 2.5.3.

Finally, the ‘classical’ NLS was applied for the same narrow spectral interval so that its result can be compared to the  
linear fit. The outcome is depicted in Fig. 13c with the methane source clearly identified. Compared to the linear setup, the  
nonlinear fits are more sensitive to variations in albedo but yield a smaller bias. The relative enhancement is slightly better  
425 represented in Fig. 13a. However, in contrast to the linear fits the NLS fit is able to detect  $\text{CH}_4$  enhancements for large intervals  
of several hundred wavenumbers (see Sec. 3.1.2). The analysis also showed that the albedo induced variations in the NLS  
are less pronounced in scene 11 which was observed at approximately twice the altitude. However, the impact of decreasing  
ground pixel resolution from higher altitudes on inferred enhancements was also recognized.

### 3.2 Matched Filter

430 The classical and cluster tuned matched filter was examined for scene 09. Both variants clearly identifies the methane plume,  
however, as shown in Fig. 14 the cluster tuning is beneficial in reducing the interference of the plume signal with surface  
reflectivity.



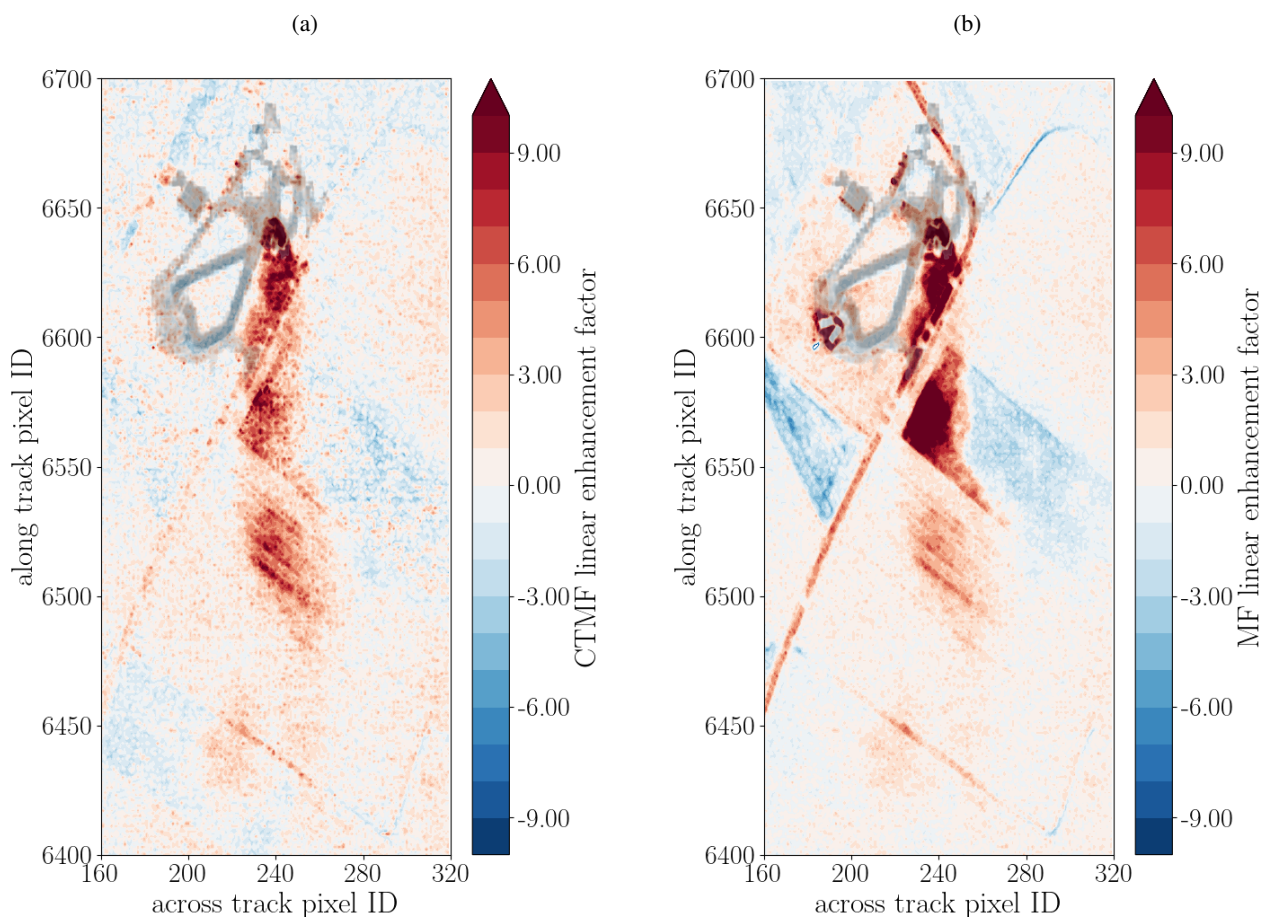


**Figure 14.** (a) Cluster tuned matched filter and (b) classical matched filter fits from  $4150\text{--}4900\text{ cm}^{-1}$ . The enhancement factor indicates the number of mixing ratio length (390 ppm m) found in the observed spectrum by scaling its Jacobian (see Eq. 16).

### 3.3 Singular Value Decomposition

The retrieval of  $\text{CH}_4$  via the SVD based method in Fig. 15 can clearly identify the methane plume. The method yields consistent  
435 results for both spectral intervals. The retrieval setup employed the first four base vectors and the  $\text{CH}_4$  Jacobian (see Fig. 7) in the linear least squares fit. Other combinations were tested but higher order base vectors were found to interfere with the methane signal so that this one turned out to give best results when using the  $\text{CH}_4$  Jacobian from the model output. The plume was also identified for the purely ‘data-driven’ approach, i. e., where the SVD base vector that mimics the  $\text{CH}_4$  absorption is used as the target signature (and does not require the forward model’s Jacobian).



440 It was found that cluster tuning significantly improves the results when only four base vectors plus the model Jacobian are used. The reason is that variance within each cluster is smaller. Moreover, the cluster tuning is beneficial in reducing the interference of the plume signal with surface reflectivity.

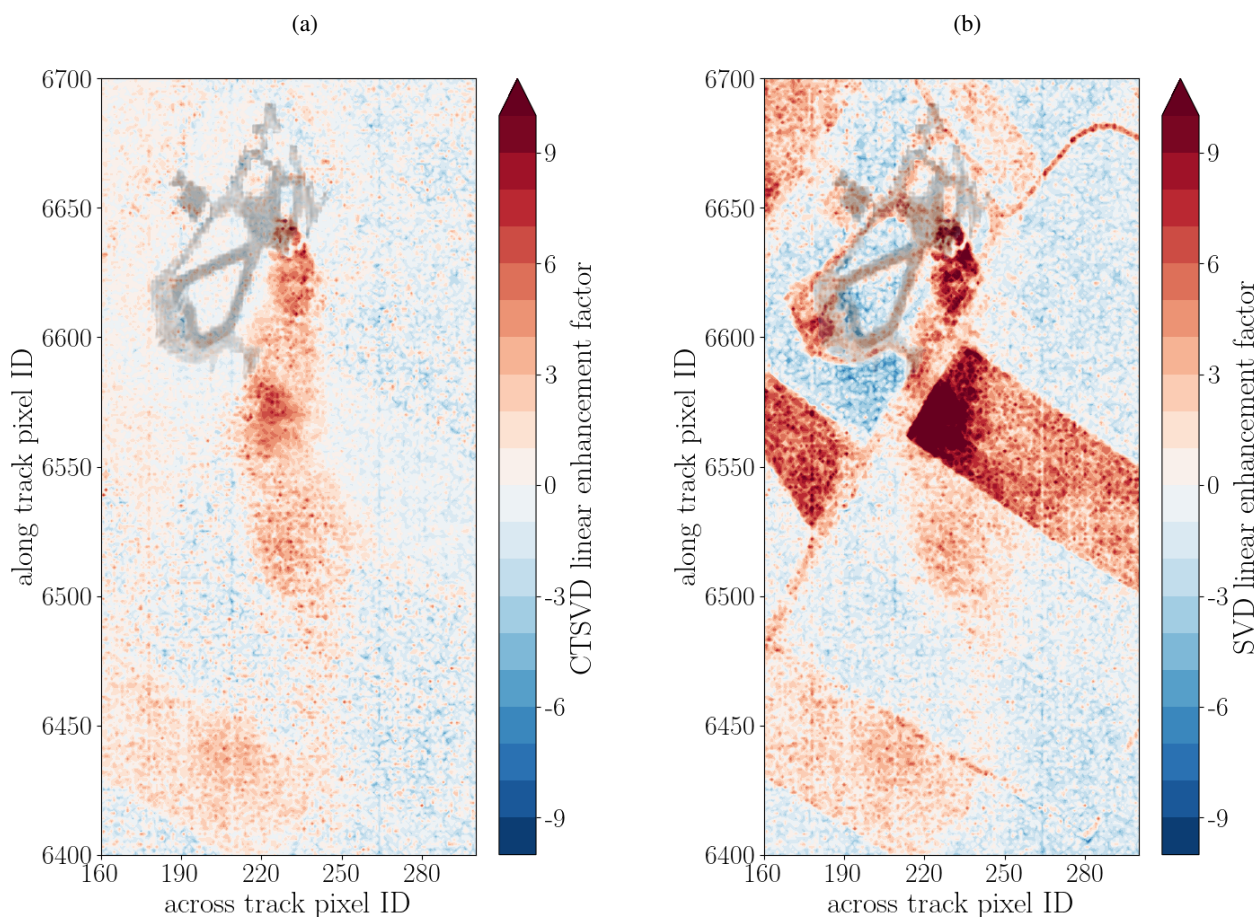


**Figure 15.** (a) Cluster tuned background SVD and (b) background SVD fits from  $5700\text{--}6300\text{cm}^{-1}$ . Same as in the MF fit, the enhancement factor indicates the number of reference plumes mixing ratios found in the observed signal. Methane Jacobian was calculated for lowest 2km (the plume component).

### 3.4 SSD

445 Finally, the SSD method for the detection of enhanced methane concentrations (see Sec. 2.5.3) is assessed. Figure 16 shows the output from Eq. 23 for a zero (a,d,g), first (b,e,h) and second order (c,f,i) polynomial, respectively. The range of the spectral interval upon which the polynomials are fitted vary so that  $5960\text{--}6040\text{cm}^{-1}$ ,  $5940\text{--}6070\text{cm}^{-1}$ , and  $5920\text{--}6090\text{cm}^{-1}$  applies, respectively. The zero order polynomial (a constant—the mean) is rather sensitive to the chosen out-band pixels and only one



or two neighboring out-band pixels should be chosen for the polynomial fit. The higher order fits, in particular the second order, was much less sensitive to the chosen bounds of the interval and yielded enhanced in-band residuals also for larger intervals. Moreover, because the out-band polynomial should capture the reflectivity and (known / not varying) absorption of the interfering molecules (i. e. H<sub>2</sub>O and CO<sub>2</sub>) a polynomial up to second order was considered appropriate from the physical perspective. Fig. 16 clearly demonstrated that the second order polynomial is mandatory to capture the surface reflectivity.

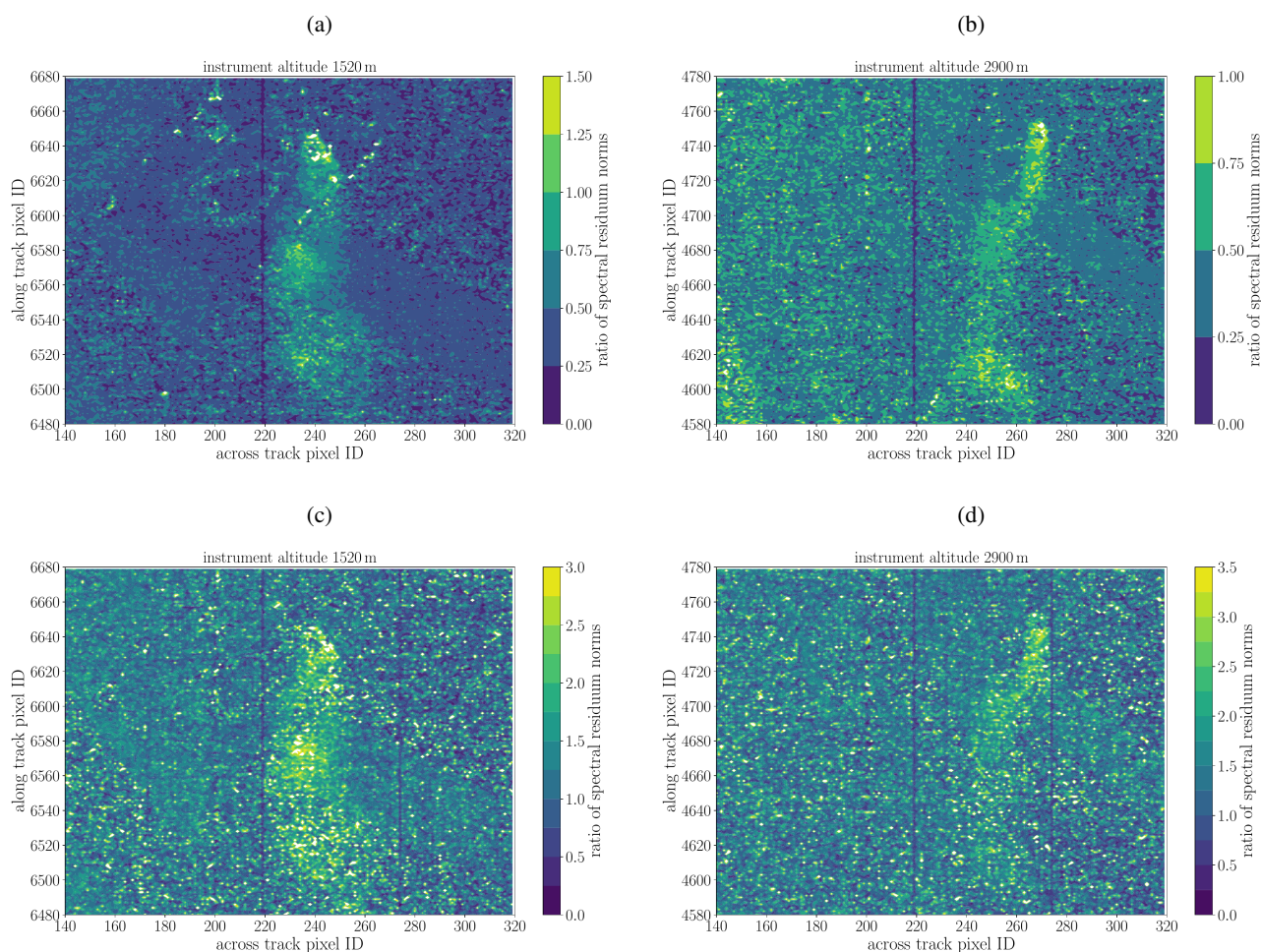


**Figure 16.** The figure depicts results for scene 09 over Pniovek V in the left column and observations from scene 11 from 2.9 km altitude in the right column. The ratio of the spectral residuals for the in- and out-band pixel is depicted. In (a) and (b) residuals with respect to a mean (a model represented by a constant) from 5960–6040 cm<sup>-1</sup> are shown while in the second row the fit results for a quadratic polynomial from 5940–6070 cm<sup>-1</sup> is depicted.

The results show that all three polynomials are able to detect the enhanced CH<sub>4</sub> absorption but also indicate that the constant and second order polynomial are best in capturing features from surface reflectivity. In Fig. 16 also the zero and first order





455 polynomial are able to capture most of the surface reflectivity features, although the signal of the plume is relatively weak in  
the center plots. This result shows that the better the ground resolution (lower flight altitude) the more sensitive the residuals  
become to albedo variations and the higher the degree of the polynomial should be chosen.

#### 4 Discussions

A validation from independent measurements is hence outside the scope of this study and should be examined in a dedicated  
460 effort. Although measurements were taken in the Katowice area on June 7th by other instruments, none was made in the very  
proximity of the shafts (see Luther et al. (2022)). Nonetheless, the results from the well established MF method can be con-  
sidered some sort of verification. Moreover, the SVD and MF methods were also examined with signatures from independent  
spectral unmixing algorithms and the results agreed well with  $\approx 3\%$ . As indicated in Luther et al. (2022, Fig. 4 and 6) wind  
was present from easterly directions which is in good alignment with the drift of the detected plume (also see Luther et al.  
465 (2022, Fig. 4 and 6) and Fig. 1b).

The BIRRA setup utilizing the scenes background pixel (observations not impacted by the methane plume) covariance  
statistics was found to be the most sensitive method for the detection of enhanced methane, although concentration within the  
plume is 2-3 times larger than for the classical least squares setup. So for investigating methane emissions at known locations  
this method is well applicable as its slow speed is not of much concern for some thousands of observations. However, when  
470 examining for potential  $\text{CH}_4$  leakages on large datasets the linear solvers such as the SVD or MF are much more adequate  
due to their significant better speed performance. Spectral clustering of the background pixels revealed to improve the retrieval  
results of the linear methods by reducing the correlation of  $\text{CH}_4$  with surface reflectivity. This is in good agreement with  
findings by Nesme et al. (2020).

So far only narrow retrieval intervals were used for the linearized BIRRA scheme but with some foreseen modifications a  
475 setup that allows for large and even multi interval setups is under investigation.

#### 5 Conclusions

The study examines the feasibility of methane retrievals from hyperspectral imaging observations using various retrieval meth-  
ods. It was found that localized  $\text{CH}_4$  enhancements close to the ground can be detected and potentially quantified from HySpex  
airborne observations.

480 The BIRRA NLS fit turned out to be sensitive to spectral variations in the albedo which induced surface-type dependent  
(positive and negative) biases, an effect that was described by many studies using data from similar hyperspectral sensors  
(Borchardt et al., 2021). The albedo related correlation was also found in the single retrieval window solutions of the SLS fit,  
although it splits (separates) the nonlinear from linear (reflectivity) parameters. The effect was dominant for single spectral  
intervals but less pronounced when multiple intervals were chosen for the fit (e. g. 4K and 6K combined). The multiwindow  
485 fits yielded retrieval errors below the maximum encountered enhancements which can be regarded significant. The GLS fit





significantly reduced the albedo bias and appears to be less influenced by the underlying surface-type. Moreover, this setup enhances the actual methane signal so that a well pronounced CH<sub>4</sub> plume is inferred. The two- to three times higher methane concentrations diminish to a one- or twofold difference when adding the surface related biases in the classical retrieval setups.

The linear estimators turned out to be very fast and hence good for near real time processing of large hyperspectral datasets. The well established MF method for hyperspectral data agree well on the enhancement pattern and confirmed the BIRRA results. The SVD based fit confirmed the results and underlined that the identified enhancement resembles an increased signal of methane absorption. Both linear methods yielded increased performance when the scene was further divided into clusters by applying k-means in a preprocessing step. Another important finding is that both linear methods, SVD and MF, agree well on the plume's shape. It is important to note that the MF yields 50–100 % higher enhancement factors compared to the SVD method which is attributed to the background covariance exploited in the MF method—a behavior also observed in the nonlinear fits.

The linear BIRRA setup was able to detect (and preliminary quantify) CH<sub>4</sub> enhancements, particularly in the wavenumber region around 6000 cm<sup>-1</sup>. However, the linear results are sensitive to the selected combination of spectral interval and state vector. This is also attributed to degeneracies between the surface reflectivity and the broad band molecular absorption features. The linearized forward model also tends to underestimate enhancements which agrees well with findings from Borchardt et al. (2021). In general, narrow retrieval intervals with only one reflectivity coefficient in the state vector turned out to constitute a stable retrieval setup in terms of detecting CH<sub>4</sub> enhancements. Nonetheless, it is a very fast retrieval scheme that can process scenes in near real time and simulations (not shown) indicated that the results improve for instruments with higher spectral resolutions so that the linear scheme should definitely be studied for measurements from other sensors.

Another simple yet effective method for detecting increased levels of methane is the SSD method. It detects relative enhancements and might serve as a real time (onboard/inflight) analysis tool for uncalibrated spectra. The detection method was able to pinpoint the source over various active shafts. Similar to the linear fit, it yielded best results for small intervals around 6000 cm<sup>-1</sup>. As pointed out by Thompson et al. (2015) those linear methods should be considered complementary to other more complete retrieval algorithms such as BIRRA.

The sensitivity study of retrieval parameters with respect to different SNRs showed that the nonlinear and separable fits rather perform similar for different state vectors. It was shown that low SNRs in the measurement spectrum make the co-retrieval of aerosol optical depth together with a (high order) reflectivity polynomial challenging, rather impossible.

In conclusion, the presented methods are suitable to detect methane enhancements from hyperspectral SWIR observations at high spatial resolution. Moreover, the new Python version of the BIRRA code which uses Py4CATS as its forward model turned out to be a flexible toolbox for prototyping.

In accordance with Guanter et al. (2021) the brightness and homogeneity of the surface are major drivers for the detection and quantification of methane plumes. Also Borchardt et al. (2021) found that the retrieved total columns suffer from retrieval noise which varies significantly over different surface-types. The study also found large discrepancies in the fitted total columns of two different retrieval algorithms. It also showed that strict filtering might allow to provide enhancement values necessary to calculate fluxes although the absolute concentrations retrieved using the different methods need to be assessed in a separate



validation study. Although greenhouse gas observations from HySpex-like sensors are challenging primarily due to its low spectral resolution further studies should investigate the potential for leakage mapping. In a next step, which is outside the scope of this study, the estimation of emission rates should be studied. Furthermore, methods specific to imaging spectrometer data such as spectral unmixing can be tested as an alternative preprocessing steps to cluster the scene for subsequent CH<sub>4</sub> retrievals based on the MF or SVD as it removes clutter while keeping unaltered the spectral information from the methane plume.

*Code availability.* The forward model is available via the Py4CA<sub>T</sub>S (Schreier et al., 2019) software suite under <https://atmos.eoc.dlr.de/tools/Py4CA<sub>T</sub>S/index.html>.

*Data availability.* On request

*Author contributions.* Philipp Hochstaffl (PH) developed and implemented the retrieval setups, ran all retrievals and wrote the manuscript. Franz Schreier (FS) originally designed and developed the software package Py4CA<sub>T</sub>S and supported the data evaluation. Claas Köhler (CK) conceived the experimental setup and conducted the data acquisition of the airborne measurements. Andreas Baumgartner (AB) performed the instrument calibration and Level 0-1 processing. CK, AB contributed the experimental setup to the manuscript. Daniele Cerra (DC) gave valuable advice for the cluster tuning approach and provided spectral unmixing data for the verification of the SVD and MF results. All authors reviewed the manuscript.

*Competing interests.* The authors declare that they have no conflict of interest.

*Acknowledgements.* We thank Thomas Trautmann and Peter Haschberger for valuable criticism of the manuscript. Furthermore we thank Konstantin Gerilowski for initiating cooperation with the CoMet campaign and Andreas Fix as the campaign leader for the support and coordination.



## 540 References

- Anderson, G., Clough, S., Kneizys, F., Chetwynd, J., and Shettle, E.: AFGL atmospheric constituent profiles (0 - 120 km), Tech. Rep. TR-86-0110, AFGL, 1986.
- Baumgartner, A.: Traceable imaging spectrometer calibration and transformation of geometric and spectral pixel properties, Ph.D. thesis, <https://doi.org/10.48693/38>, 2021.
- 545 Baumgartner, A. and Köhler, C. H.: Transformation of point spread functions on an individual pixel scale, *Optics Express*, 28, 38 682–38 697, <https://doi.org/10.1364/oe.409626>, tex.date\_added: Tue Dec 15 16:52:19 2020, 2020.
- Borchardt, J., Gerilowski, K., Krautwurst, S., Bovensmann, H., Thorpe, A. K., Thompson, D. R., Frankenberg, C., Miller, C. E., Duren, R. M., and Burrows, J. P.: Detection and quantification of CH<sub>4</sub> plumes using the WFM-DOAS retrieval on AVIRIS-NG hyperspectral data, *Atmos. Meas. Tech.*, 14, 1267–1291, <https://doi.org/10.5194/amt-14-1267-2021>, 2021.
- 550 Buchwitz, M., Rozanov, V., and Burrows, J.: A near-infrared optimized DOAS method for the fast global retrieval of atmospheric CH<sub>4</sub>, CO, CO<sub>2</sub>, H<sub>2</sub>O, and N<sub>2</sub>O total column amounts from SCIAMACHY Envisat-1 nadir radiances, *J. Geophys. Res.*, 105, 15 231–15 245, <https://doi.org/10.1029/2000JD900191>, 2000.
- Buchwitz, M., de Beek, R., Bramstedt, K., Noël, S., Bovensmann, H., and Burrows, J. P.: Global carbon monoxide as retrieved from SCIAMACHY by WFM-DOAS, *Atm. Chem. Phys.*, 4, 1945–1960, <https://doi.org/10.5194/acp-4-1945-2004>, 2004.
- 555 Buchwitz, M., de Beek, R., Noël, S., Burrows, J. P., Bovensmann, H., Bremer, H., Bergamaschi, P., Körner, S., and Heimann, M.: Carbon monoxide, methane and carbon dioxide columns retrieved from SCIAMACHY by WFM-DOAS: year 2003 initial data set, *Atm. Chem. Phys.*, 5, 3313–3329, <https://doi.org/10.5194/acp-5-3313-2005>, 2005.
- Chabrilat, S., Guanter, L., Segl, K., Foerster, S., Fischer, S., Rossner, G., Schickling, A., LaPorta, L., Honold, H.-P., and Storch, T.: The Enmap German Spaceborne Imaging Spectroscopy Mission: Update and Highlights of Recent Preparatory Activities, in: *IGARSS 2020 - 2020 IEEE Intern. Geosci. and Remote Sens. Symposium*, pp. 3278–3281, <https://doi.org/10.1109/IGARSS39084.2020.9324006>, 2020.
- 560 De Leeuw, G., Kinne, S., Léon, J.-F., Pelon, J., Rosenfeld, D., Schaap, M., Veeffkind, P. J., Veihelmann, B., Winker, D. M., and Von Hoyningen-Huene, W.: Retrieval of Aerosol Properties, in: *The Remote Sensing of Tropospheric Composition from Space*, edited by John P. Burrows, U. P. and Borrell, P., *Phys. of Earth and Space Environ.*, pp. 259–313, Springer-Verlag, [https://doi.org/10.1007/978-3-642-14791-3\\_6](https://doi.org/10.1007/978-3-642-14791-3_6), 2011.
- 565 Delahaye, T., Armante, R., Scott, N., Jacquinet-Husson, N., Chédin, A., Crépeau, L., Crevoisier, C., Douet, V., Perrin, A., Barbe, A., Boudon, V., Campargue, A., Coudert, L., Ebert, V., Flaud, J.-M., Gamache, R., Jacquemart, D., Jolly, A., Kwabia Tchana, F., Kyuberis, A., Li, G., Lyulin, O., Manceron, L., Mikhailenko, S., Moazzen-Ahmadi, N., Müller, H., Naumenko, O., Nikitin, A., Perevalov, V., Richard, C., Starikova, E., Tashkun, S., Tyuterev, V., Vander Auwera, J., Vispoel, B., Yachmenev, A., and Yurchenko, S.: The 2020 edition of the GEISA spectroscopic database, *J. Mol. Spectrosc.*, 380, 111 510, <https://doi.org/https://doi.org/10.1016/j.jms.2021.111510>, 2021.
- 570 Frankenberg, C., Platt, U., and Wagner, T.: Retrieval of CO from SCIAMACHY onboard ENVISAT: detection of strongly polluted areas and seasonal patterns in global CO abundances, *Atm. Chem. Phys.*, 5, 1639–1644, <https://doi.org/10.5194/acp-5-1639-2005>, 2005.
- Funk, C., Theiler, J., Roberts, D., and Borel, C.: Clustering to improve matched filter detection of weak gas plumes in hyperspectral thermal imagery, *IEEE Transactions on Geoscience and Remote Sensing*, 39, 1410–1420, <https://doi.org/10.1109/36.934073>, 2001.
- Gerilowski, K., Tretner, A., Krings, T., Buchwitz, M., Bertagnolio, P. P., Belemezov, F., Erzinger, J., Burrows, J. P., and Bovensmann, H.: MAMAP – a new spectrometer system for column-averaged methane and carbon dioxide observations from aircraft: instrument description and performance analysis, *Atmos. Meas. Tech.*, 4, 215–243, <https://doi.org/10.5194/amt-4-215-2011>, 2011.



- Gimeno García, S., Schreier, F., Lichtenberg, G., and Slijkhuis, S.: Near infrared nadir retrieval of vertical column densities: methodology and application to SCIAMACHY, *Atmos. Meas. Tech.*, 4, 2633–2657, <https://doi.org/10.5194/amt-4-2633-2011>, 2011.
- 580 Golub, G. and Pereyra, V.: Separable nonlinear least squares: the variable projection method and its applications, *Inverse Problems*, 19, R1–R26, <https://doi.org/10.1088/0266-5611/19/2/201>, 2003.
- Green, R. O., Carrere, V., and Conel, J. E.: Measurement of atmospheric water vapor using the Airborne Visible/Infrared Imaging Spectrometer, in: *ASPRS Conference on ImageProcessing*, pp. 73–76, 1989.
- Green, R. O., Eastwood, M. L., Sarture, C. M., Chrien, T. G., Aronsson, M., Chippendale, B. J., Faust, J. A., Pavri, B. E., Chovit, C. J., Solis, M., Olah, M. R., and Williams, O.: Imaging Spectroscopy and the Airborne Visible/Infrared Imaging Spectrometer (AVIRIS), *Remote Sensing of Environment*, 65, 227–248, [https://doi.org/https://doi.org/10.1016/S0034-4257\(98\)00064-9](https://doi.org/https://doi.org/10.1016/S0034-4257(98)00064-9), 1998.
- 585 Guanter, L., Irakulis-Loitxate, I., Gorroño, J., Sánchez-García, E., Cusworth, D. H., Varon, D. J., Cogliati, S., and Colombo, R.: Mapping methane point emissions with the PRISMA spaceborne imaging spectrometer, *Remote Sensing of Environment*, 265, 112 671, <https://doi.org/https://doi.org/10.1016/j.rse.2021.112671>, 2021.
- Hansen, P., Pereyra, V., and Scherer, G.: *Least Squares Data Fitting with Applications*, Johns Hopkins University Press, 2013.
- 590 Hochstaff, P. and Schreier, F.: Impact of Molecular Spectroscopy on Carbon Monoxide Abundances from SCIAMACHY, *Remote Sens.*, 12, 1084, <https://doi.org/10.3390/rs12071084>, 2020.
- Hochstaff, P., Schreier, F., Lichtenberg, G., and Gimeno García, S.: Validation of Carbon Monoxide Total Column Retrievals from SCIAMACHY Observations with NDACC/TCCON Ground-Based Measurements, *Remote Sens.*, 10, 223, <https://doi.org/10.3390/rs10020223>, 2018.
- 595 Hochstaff, P., Schreier, F., Birk, M., Wagner, G., Feist, G. D., Notholt, J., Sussmann, R., and Té, Y.: Impact of Molecular Spectroscopy on Carbon Monoxide Abundances from TROPOMI, *Remote Sens.*, 12, 3486, <https://doi.org/10.3390/rs12213486>, 2020.
- Humpage, N., Boesch, H., Palmer, P. I., Vick, A., Parr-Burman, P., Wells, M., Pearson, D., Strachan, J., and Bezawada, N.: GreenHouse gas Observations of the Stratosphere and Troposphere (GHOST): an airborne shortwave-infrared spectrometer for remote sensing of greenhouse gases, *Atmos. Meas. Tech.*, 11, 5199–5222, <https://doi.org/10.5194/amt-11-5199-2018>, 2018.
- 600 (IMF), D. R. S. T. I.: Airborne imaging spectrometer HySpex, *Journal of large-scale research facilities*, 2, 1–6, <https://doi.org/10.17815/jlsrf-2-151>, 2016.
- Intergovernmental Panel on Climate Change: *Climate Change 2013 – The Physical Science Basis: Working Group I Contribution to the Fifth Assessment Report of the Intergovernmental Panel on Climate Change*, Cambridge University Press, <https://doi.org/10.1017/CBO9781107415324>, 2014.
- 605 Jervis, D., McKeever, J., Durak, B. O. A., Sloan, J. J., Gains, D., Varon, D. J., Ramier, A., Strupler, M., and Tarrant, E.: The GHGSat-D imaging spectrometer, *Atmos. Meas. Tech.*, 14, 2127–2140, <https://doi.org/10.5194/amt-14-2127-2021>, 2021.
- Kalnay, E., Kanamitsu, M., Kistler, R., Collins, W., Deaven, D., Gandin, L., Iredell, M., Saha, S., White, G., Woollen, J., Zhu, Y., Chelliah, M., Ebisuzaki, W., Higgins, W., Janowiak, J., Mo, K. C., Ropelewski, C., Wang, J., Leetmaa, A., Reynolds, R., Jenne, R., and Joseph, D.: The NCEP/NCAR 40-Year Reanalysis Project, *Bull. Am. Met. Soc.*, 77, 437–472, [https://doi.org/10.1175/1520-0477\(1996\)077<0437:TNYRP>2.0.CO;2](https://doi.org/10.1175/1520-0477(1996)077<0437:TNYRP>2.0.CO;2), 1996.
- 610 Krings, T., Gerilowski, K., Buchwitz, M., Reuter, M., Tretner, A., Erzinger, J., Heinze, D., Pflüger, U., Burrows, J. P., and Bovensmann, H.: MAMAP — a new spectrometer system for column-averaged methane and carbon dioxide observations from aircraft: retrieval algorithm and first inversions for point source emission rates, *Atmos. Meas. Tech.*, 4, 1735–1758, <https://doi.org/10.5194/amt-4-1735-2011>, 2011.



- 615 Kuze, A., Suto, H., Nakajima, M., and Hamazaki, T.: Thermal and near infrared sensor for carbon observation Fourier-transform spectrometer on the Greenhouse Gases Observing Satellite for greenhouse gases monitoring, *Appl. Opt.*, 48, 6716–6733, <https://doi.org/10.1364/AO.48.006716>, 2009.
- Kuze, A., Suto, H., Shiomi, K., Kawakami, S., Tanaka, M., Ueda, Y., Deguchi, A., Yoshida, J., Yamamoto, Y., Kataoka, F., Taylor, T. E., and Buijs, H. L.: Update on GOSAT TANSO-FTS performance, operations, and data products after more than 6 years in space, *Atmos. Meas. Tech.*, 9, 2445–2461, <https://doi.org/10.5194/amt-9-2445-2016>, 2016.
- 620 Lauvaux, T., Giron, C., Mazzolini, M., d’Aspremont, A., Duren, R., Cusworth, D., Shindell, D., and Ciais, P.: Global assessment of oil and gas methane ultra-emitters, *Science*, 375, 557–561, <https://doi.org/10.1126/science.abj4351>, 2022.
- Lenhard, K., Baumgartner, A., and Schwarzaier, T.: Independent laboratory characterization of neo HySpex imaging spectrometers VNIR-1600 and SWIR-320m-e, *IEEE Transactions on Geoscience and Remote Sensing*, 53, 1828–1841, <https://doi.org/10.1109/tgrs.2014.2349737>, tex.date\_added: Fri May 24 16:15:14 2019, 2015.
- 625 Liou, K.-N.: *An Introduction to Atmospheric Radiation*, Academic Press, second edn., 2002.
- Lorente, A., Borsdorff, T., Butz, A., Hasekamp, O., aan de Brugh, J., Schneider, A., Wu, L., Hase, F., Kivi, R., Wunch, D., Pollard, D. F., Shiomi, K., Deutscher, N. M., Velasco, V. A., Roehl, C. M., Wennberg, P. O., Warneke, T., and Landgraf, J.: Methane retrieved from TROPOMI: improvement of the data product and validation of the first 2 years of measurements, *Atmos. Meas. Tech.*, 14, 665–684, <https://doi.org/10.5194/amt-14-665-2021>, 2021.
- 630 Luther, A., Kleinschek, R., Scheidweiler, L., Defratyka, S., Stanisavljevic, M., Forstmaier, A., Dandocsi, A., Wolff, S., Dubravica, D., Wildmann, N., Kostinek, J., Jöckel, P., Nickl, A.-L., Klausner, T., Hase, F., Frey, M., Chen, J., Dietrich, F., Necki, J., Swolkieñ, J., Fix, A., Roiger, A., and Butz, A.: Towards verifying CH<sub>4</sub> emissions from hard coal mines using mobile sun-viewing Fourier transform spectrometry, *Atmos. Meas. Tech. Disc.*, 2019, 1–19, <https://doi.org/10.5194/amt-2019-205>, 2019.
- Luther, A., Kostinek, J., Kleinschek, R., Defratyka, S., Stanisavljević, M., Forstmaier, A., Dandocsi, A., Scheidweiler, L., Dubravica, D., 635 Wildmann, N., Hase, F., Frey, M. M., Chen, J., Dietrich, F., Necki, J., Swolkieñ, J., Knot, C., Vardag, S. N., Roiger, A., and Butz, A.: Observational constraints on methane emissions from Polish coal mines using a ground-based remote sensing network, *Atmospheric Chemistry and Physics*, 22, 5859–5876, <https://doi.org/10.5194/acp-22-5859-2022>, publisher: Copernicus GmbH, 2022.
- Masson-Delmotte, V., Zhai, P., Pirani, A., Connors, S., Péan, C., Berger, S., Caud, N., Chen, Y., Goldfarb, L., Gomis, M., Huang, M., Leitzell, K., Lonnoy, E., Matthews, J., Maycock, T., Waterfield, T., Yelekçi, O., Yu, R., and (eds.), B. Z.: *Climate Change 2021: The Physical Science Basis. Contribution of Working Group I to the Sixth Assessment Report of the Intergovernmental Panel on Climate Change*, Cambridge University Press, <https://doi.org/10.1017/CBO9781107415324>, 2021.
- 640 Nesme, N., Foucher, P.-Y., and Doz, S.: Detection and quantification of industrial methane plume with the airborne Hypspx-NEO camera and applications to satellite data, in: XXIV ISPRS Congress 2020 edition, vol. XLIII-B3-2020, pp. 821 – 827, Online, France, <https://doi.org/10.5194/isprs-archives-xxiii-b3-2020-821-2020>, 2020.
- 645 Nickl, A.-L., Mertens, M., Roiger, A., Fix, A., Amediek, A., Fiehn, A., Gerbig, C., Galkowski, M., Kerkweg, A., Klausner, T., Eckl, M., and Jöckel, P.: Hindcasting and forecasting of regional methane from coal mine emissions in the Upper Silesian Coal Basin using the online nested global regional chemistry–climate model MECO(n) (MESSy v2.53), *Geoscientific Model Development*, 13, 1925–1943, <https://doi.org/10.5194/gmd-13-1925-2020>, 2020.

OpenStreetMap contributors 2022: Distributed under the Open Data Commons Open Database License (ODbL) v1.0.



- 650 Pandya, M. R., Chhabra, A., Pathak, V. N., Trivedi, H., and Chauhan, P.: Mapping of thermal power plant emitted atmospheric carbon dioxide concentration using AVIRIS-NG data and atmospheric radiative transfer model simulations, *J. Appl. Remote Sens.*, 15, <https://doi.org/10.1117/1.jrs.15.032204>, 2021.
- Richter, A.: Satellite remote sensing of tropospheric composition - principles, results, and challenges, *EPJ Web of Conferences*, 9, 181–189, <https://doi.org/10.1051/epjconf/201009014>, 2010.
- 655 Schneising, O., Buchwitz, M., Burrows, J. P., Bovensmann, H., Bergamaschi, P., and Peters, W.: Three years of greenhouse gas column-averaged dry air mole fractions retrieved from satellite — Part 2: Methane, *Atm. Chem. Phys.*, 9, 443–465, <https://doi.org/10.5194/acp-9-443-2009>, 2009.
- Schreier, F., Gimeno García, S., Hedelt, P., Hess, M., Mendrok, J., Vasquez, M., and Xu, J.: GARLIC – A General Purpose Atmospheric Radiative Transfer Line-by-Line Infrared-Microwave Code: Implementation and Evaluation, *J. Quant. Spectrosc. & Radiat. Transfer*, 137, 29–50, <https://doi.org/10.1016/j.jqsrt.2013.11.018>, 2014.
- 660 Schreier, F., Gimeno García, S., Hochstaffl, P., and Städt, S.: Py4CAAtS — PYthon for Computational ATmospheric Spectroscopy, *Atmosphere*, 10, 262, <https://doi.org/10.3390/atmos10050262>, 2019.
- Theiler, J. and Foy, B.: Effect of signal contamination in matched-filter detection of the signal on a cluttered background, *Geosci. Remote Sens. Letters*, 3, 98–102, <https://doi.org/10.1109/LGRS.2005.857619>, 2006.
- 665 Thompson, D. R., Leifer, I., Bovensmann, H., Eastwood, M., Fladland, M., Frankenberg, C., Gerilowski, K., Green, R. O., Kratwurst, S., Krings, T., Luna, B., and Thorpe, A. K.: Real-time remote detection and measurement for airborne imaging spectroscopy: a case study with methane, *Atmos. Meas. Tech.*, 8, 4383–4397, <https://doi.org/10.5194/amt-8-4383-2015>, 2015.
- Thompson, D. R., Thorpe, A. K., Frankenberg, C., Green, R. O., Duren, R., Guanter, L., Hollstein, A., Middleton, E., Ong, L., and Ungar, S.: Space-based remote imaging spectroscopy of the Aliso Canyon CH<sub>4</sub> superemitter, *Geophys. Res. Letters*, 43, 6571–6578, <https://doi.org/https://doi.org/10.1002/2016GL069079>, 2016.
- 670 Thorndike, R. L.: Who belongs in the family, *Psychometrika*, pp. 267–276, 1953.
- Thorpe, A. K., Roberts, D. A., Bradley, E. S., Funk, C. C., Dennison, P. E., and Leifer, I.: High resolution mapping of methane emissions from marine and terrestrial sources using a Cluster-Tuned Matched Filter technique and imaging spectrometry, *Remote Sensing of Environment*, 134, 305–318, <https://doi.org/https://doi.org/10.1016/j.rse.2013.03.018>, 2013.
- 675 Thorpe, A. K., Frankenberg, C., and Roberts, D. A.: Retrieval techniques for airborne imaging of methane concentrations using high spatial and moderate spectral resolution: application to AVIRIS, *Atmos. Meas. Tech.*, 7, 491–506, <https://doi.org/10.5194/amt-7-491-2014>, 2014.
- United Nations Framework Convention on Climate: Paris Agreement to the United Nations Framework Convention on Climate Change, [https://unfccc.int/files/meetings/paris\\_nov\\_2015/application/pdf/paris\\_agreement\\_english\\_.pdf](https://unfccc.int/files/meetings/paris_nov_2015/application/pdf/paris_agreement_english_.pdf), accessed: 2021-04-01, 2015.
- Varon, D. J., McKeever, J., Jervis, D., Maasackers, J. D., Pandey, S., Houweling, S., Aben, I., Scarpelli, T., and Jacob, D. J.: Satellite Discovery of Anomalously Large Methane Point Sources From Oil/Gas Production, *Geophys. Res. Letters*, 46, 13 507–13 516, <https://doi.org/https://doi.org/10.1029/2019GL083798>, 2019.
- 680 Veefkind, J., Aben, I., McMullan, K., Förster, H., de Vries, J., Otter, G., Claas, J., Eskes, H., de Haan, J., Kleipool, Q., van Weele, M., Hasekamp, O., Hoogeveen, R., Landgraf, J., Snel, R., Tol, P., Ingmann, P., Voors, R., Kruizinga, B., Vink, R., Visser, H., and Levelt, P.: TROPOMI on the ESA Sentinel-5 Precursor: A GMES mission for global observations of the atmospheric composition for climate, air quality and ozone layer applications, *Remote Sensing of Environment*, 120, 70 – 83, <https://doi.org/10.1016/j.rse.2011.09.027>, the Sentinel Missions - New Opportunities for Science, 2012.
- 685



- Villeneuve, P. V., Fry, H. A., Theiler, J. P., Clodius, W. B., Smith, B. W., and Stocker, A. D.: Improved matched-filter detection techniques, in: *Imaging Spectrometry V*, edited by Descour, M. R. and Shen, S. S., vol. 3753, pp. 278 – 285, International Society for Optics and Photonics, Proc. SPIE, <https://doi.org/10.1117/12.366290>, 1999.
- 690 Zdunkowski, W., Trautmann, T., and Bott, A.: *Radiation in the Atmosphere: A Course in Theoretical Meteorology*, Cambridge University Press, 2007.